Comput. Methods Appl. Mech. Engrg. 199 (2010) 734–754

Contents lists available at ScienceDirect

Comput. Methods Appl. Mech. Engrg.

journal homepage: www.elsevier.com/locate/cma

Numerical aspects in the finite element simulation of the Portevin–Le Chatelier effect

M. Mazière [a,*], J. Besson [a], S. Forest [a], B. Tanguy [a], H. Chalons [b], F. Vogel [b]

[a] MINES ParisTech, Centre des Matériaux, CNRS UMR 7633, BP 87, 91003 Evry Cedex, France
[b] TURBOMECA F-64511 BORDES, France

ARTICLE INFO

Article history:
Received 5 June 2009
Received in revised form 2 November 2009
Accepted 5 November 2009
Available online 12 November 2009

Keywords:
Portevin–Le Chatelier effect
Computational mechanics
Mesh sensitivity
Viscoplastic instability

ABSTRACT

Serrated yielding and propagation of localized bands of plastic strain rate are the apparent phenomena of the Portevin–Le Chatelier (PLC) effect. The finite element modeling of this effect is investigated, using a model proposed by Zhang et al. [74] describing dynamic strain aging, and material parameters for a Nickel based superalloy at 500 °C. This work presents: (1) an efficient implicit integration scheme of the constitutive equations in the presence of instabilities; (2) a numerical tool to determine the type of plastic strain rate localization bands based on results of simulations; and (3) a mesh and time discretization sensitivity analysis of the model regarding the characteristics of PLC bands. This analysis is carried out in 2D and 3D for axisymmetric smooth and notched specimens.

1. Introduction

The Portevin–Le Chatelier (PLC) effect is associated with serrations on the macroscopic load/displacement tensile curve and with the repeated propagation of bands of localized plastic strain rate in test specimens [46,45,8]. These effects are due to dynamic strain ageing (DSA). DSA can be associated with a negative strain rate sensitivity (SRS) [58] of the material in some range of strain rate and temperature, which can be evidenced by performing tensile tests at various constant strain rates or various temperatures. At a microscopic scale, DSA is related to dynamic interactions between mobile dislocations and diffusion processes of solute atoms [23,72]. Depending on strain rate, the PLC effect starts at a more or less high strain value, which constitutes the critical strain between stable and unstable behavior [16]. In order to understand and to simulate the PLC effect in various structures and to prevent unexpected failure associated with localized phenomena, many studies have been performed dealing with experimental observations, models, and simulations of DSA.

Many observations of the PLC effect are available in the literature since it has been discovered one century ago [46,59]. It has been mainly observed in aluminium alloys since PLC effect occurs in this kind of material at room temperature. This effect has then been observed and analyzed in AlMg alloys [26,71,44,47,74,21,9,43,48,50,42,7,39,2,24,20,38,40,18,8,1,66]; AlCu alloys [35,61,41,62]; or in some other aluminium alloys [59,33,22,36], and even in metal matrix composites [57,24,34]. It has also been detected at higher temperatures (around 200 °C) in iron or steels [46,49,35]. Finally, more recently, the PLC effect has been evidenced around 500 °C in some Nickel based superalloys for aeronautical and nuclear applications [25,63,28,32,51,31,52].

Two main theoretical models for dynamic strain ageing have been developed about twenty years ago to reproduce the serrated yielding and strain rate band localization. The first one, denoted KE model, presented in [45], is based on an explicit mathematical description of negative SRS. It has been used for numerous theoretical studies of PLC effect [58,73,29], and also for some finite element modeling simulations [71,43,7]. The second one, denoted MC model, proposed in [55], and improved by [56] is a macroscopic model based on a microscopic description of the DSA introducing an internal variable t_a called ageing time. It has been used in almost all recent numerical simulations of the PLC effect [74,35,36,39,24,41,40,8]. A more recent model, based on a thermodynamical approach is presented in [37,65]. It has not been implemented yet for finite element modeling of DSA. Another model, based on the addition of different stresses, proposed in [19] has been used to carry out 1D numerical simulations of tensile tests. Finally a micro-mechanical model based on interactions between dislocations and solute dynamics has been proposed in [30]. This model should be useful for simulation of PLC effect at a smaller length scale than that of the simulated tensile specimens considered in this work.

The finite element method has been applied in the case of DSA to accurately reproduce experimental tensile tests and to validate material models and parameters. Some simulations have been performed in 2D [71,35,36,7,24,40], some in 3D [74,43,39,51,8].

* Corresponding author. Tel.: +33 1 60 76 30 45.
E-mail address: maziere@mat.ensmp.fr (M. Mazière).

0045-7825/$ - see front matter © 2009 Elsevier B.V. All rights reserved.
doi:10.1016/j.cma.2009.11.004

Different geometries of tensile specimens have been tested like smooth flat [71,74,43,40,24]; smooth round [74,7,39,51,8]; smooth prismatic [8]; U-notched flat [35,8]; U-notched round [7,51]; V-notched flat [36]. Application to CT specimens for the PLC effect at the crack tip can be found in [36,6].

All these simulations were performed with the finite element method, using different element types and sizes, and different integration methods for the constitutive equations, in order to accurately reproduce the serration on the global strain/stress curve, but also propagation of bands in specimens. Three main questions arise when performing such finite element simulations of the PLC effect: (i) how to develop an efficient method to locally integrate the material model constitutive equations in the presence of severe instabilities, (ii) how to characterize the type of bands and compare experiment with simulations, and (iii) how do finite element results depend on mesh size.

(i) The simulation of the PLC effect in test specimens using the KE or MC models mentioned previously requires to solve a quasi-static non-linear rate-dependent mechanical problem. In the framework of FEM, this problem can be solved using incremental procedures based on an explicit solver [7,40,8] or implicit (Newton–Raphson methods) formulation [74,43,35,36,16,13]. In both cases the constitutive equations are integrated at each Gauss point in order to evaluate the state variables at the end of each time step, and an estimate of the tangent stiffness matrix. Constitutive equations can be integrated using methods depending on the specific form of the flow rule or yield criterion [8]. Some generalized methods can also be used such as Runge–Kutta methods [60,70], or a modified mid-point scheme called Θ-method [68,3,17,27], that leads to more tedious mathematical developments. The latter method provides a better convergence of the global algorithm and requires the determination of the consistent tangent matrix. Integration of constitutive equations may become numerically difficult if large increments of internal variables occur for small time increments. Both methods have to be improved by a combination of automatic stepping and error correction. In the MC strain ageing model, both internal variables (i.e. the cumulated plastic strain p and the ageing time t_a) can undergo large local increments, that can slow down or even stop the global solution convergence. Two mixed algorithms combining Runge–Kutta and Θ-methods, associated with an automatic control of time steps, are presented here for the particular case of the MC model. Results of simulations of a plate in tension performed with these algorithms have been compared with results obtained using a Runge–Kutta local integration, and an approximate consistent tangent matrix equal to the elasticity tensor.

(ii) The main difficulty while modeling PLC effect is to accurately reproduce the load/displacement curve and plastic strain rate localization bands. The simulated load/displacement curve can be directly compared with experiments. The comparison of band characteristics is more difficult. Characteristics and kinetic parameters of bands such as type, spatial evolution, velocity, width, amount of plastic strain carried by each band, and maximum plastic strain rate, have been evaluated experimentally using different methods. The type of serrations and the motion of bands can change significantly from a given strain rate, temperature, or strain level to another. Serrations have been classified in three main types (A, B, and C), depending on their shape [47]. These types are associated with three different kinematic behaviors of plastic strain rate localization bands. It is first possible to estimate the type of bands from temporal analysis of the global stress/strain curve using multifractal analysis [48], recurrence analysis [66], or Markov processes [18]. Band characteristics may also be obtained based on spatial observations using thermal fields measured with a fast multi-detector infrared camera [49,61,50,62,1]; using optical observations associated with digital image correlation analysis [42,2,41,38,8]; or using acoustic emission (AE) and laser extensometry measures [21,20]. Finally some results on band behavior can be obtained by analyzing failure of specimens [33,28,42,38,40,31] or from tensile tests at a constant stress rate [26,44,20]. In order to accurately simulate the type of bands for each strain rate and temperature, a numerical tool that can easily evaluate band characteristics and kinematic parameters is proposed in this work. This tool mimics the measurement techniques of band location performed using laser extensometry or infrared pyrometry and provides most of band characteristics.

(iii) It is well-known in the framework of finite element modeling that simulations of strain localization phenomena induced by softening mechanisms can be mesh dependent [13], i.e. the size of localization bands decreases with element size. The mesh objectivity of DSA models has not been systematically studied in literature. An evolution of the band size with respect to the element size is given in [74]. Contrary to the results that we will present here, Zhang found a convergence of the band width with increasing the number of elements. However, Zhang does not focus on the mesh dependence of the other band characteristics such as band type, velocity, and amount of carried strain. These variables are estimated in several experimental studies [33,49,50,61,62,8], and in some simulations [7,8]. A comprehensive mesh sensitivity analysis of band types and parameters is then performed in this work. A formula relating the different parameters is proposed from the simulation results.

This work is divided into four parts. In the first one (Section 2), the different local integration methods of MC model are compared regarding simulation precision and computation time. In the second part (Section 3), the kinematic behavior of A, B, and C bands is reviewed. An original numerical tool to detect the type and kinematic parameters of a localization band is provided: the Band Location Indicator (BLI). BLI is suitable to perform a strain rate sensitivity analysis of the MC model for the simulation of a plate in tension. It is also useful to perform the detailed analysis of the mesh sensitivity of localization carried out in the third part (Section 4). The influence of element size on the critical plastic strain, serrations, band type, and kinematic band parameters, is investigated in a systematic way. Finally in Section 5, some large scale simulations on 3D smooth and notched round specimens are presented as an extension of 2D results presented in Section 4.

2. Numerical integration of MC constitutive equations

2.1. Finite element formulation

The incremental finite element resolution of non-linear mechanical problems consists in solving at each step i the following equation:

$$\begin{cases} \text{Assuming at time } t=t^i,\ \underline{\boldsymbol{F}_{int}}(\underline{\boldsymbol{u}}^i)=\underline{\boldsymbol{F}_{ext}}^i, \\ \text{Find the displacement field at time } t^{i+1},\ \underline{\boldsymbol{u}}^{i+1}=\underline{\boldsymbol{u}}^i+\Delta\underline{\boldsymbol{u}}^i \text{ such as :}, \\ \underline{\boldsymbol{F}_{int}}(\underline{\boldsymbol{u}}^{i+1})=\underline{\boldsymbol{F}_{ext}}^{i+1}. \end{cases} \tag{1}$$

where $\underline{\boldsymbol{u}}^i$ denotes the vector of nodal displacements at step i, and $\underline{\boldsymbol{F}_{int}}(\underline{\boldsymbol{u}}^i)$ and $\underline{\boldsymbol{F}_{ext}}^i$ the corresponding internal and external forces act-

ing on the discretized system. The value of external forces at step $i+1$, $\underline{\boldsymbol{F}_{ext}}^{i+1}$ is deduced from boundary conditions and loading path.

This non-linear problem can be solved at each step using iterative procedures [68,13] such as Newton–Raphson implicit methods. Introducing the shape function derivative matrix $\mathbb{B}$, for each calculation iteration k:

(a) The displacement field is updated $\Delta\underline{\boldsymbol{u}}^i_{k+1} = \Delta\underline{\boldsymbol{u}}^i_k + \delta\underline{\boldsymbol{u}}^i_k$.
(b) The strain tensor increment at each Gauss point $\Delta\underset{\sim}{\boldsymbol{\varepsilon}}^i_{k+1} = \mathbb{B}\Delta\underline{\boldsymbol{u}}^i_{k+1}$ is computed.
(c) The constitutive equations are integrated to provide the internal/state variable increments, in particular the stress tensor increment $\Delta\underset{\sim}{\boldsymbol{\sigma}}^i_{k+1}$; and the consistent tangent operator $\frac{\partial\Delta\underset{\sim}{\boldsymbol{\sigma}}^i_{k+1}}{\partial\Delta\underset{\sim}{\boldsymbol{\varepsilon}}^i_{k+1}}$.
(d) Internal forces $\underline{\boldsymbol{F}_{int}}(\underline{\boldsymbol{u}}^i + \Delta\underline{\boldsymbol{u}}^i_{k+1})$ are computed.
(e) Residual forces $\underline{\boldsymbol{R}}^i_{k+1} = \underline{\boldsymbol{F}_{int}}(\underline{\boldsymbol{u}}^i + \Delta\underline{\boldsymbol{u}}^i_{k+1}) - \underline{\boldsymbol{F}_{ext}}^{i+1}$ are computed.
(f) The new displacement increment $\delta\underline{\boldsymbol{u}}^i_{k+1} = -[\mathbb{K}^i_{k+1}]^{-1}\underline{\boldsymbol{R}}^i_{k+1}$ is computed.

This procedure ends when a given norm of residual vector $\underline{\boldsymbol{R}}^i_{k+1}$ becomes smaller than a given value $\boldsymbol{r}$ called the global convergence ratio. The stiffness matrix used in the Newton–Raphson method is:

$$\mathbb{K}^i_{k+1} = \frac{\partial\underline{\boldsymbol{F}_{int}}}{\partial\underline{\boldsymbol{u}}}(\underline{\boldsymbol{u}}^i_{k+1}) = \int_v \mathbb{B}^t\,\underset{\approx}{\boldsymbol{L}}\,\mathbb{B}dv, \tag{2}$$

where $\boldsymbol{L}$ is an estimate of the actual tangent operator $\boldsymbol{L}^i_{k+1}$. This estimate can be the tensor of elastic moduli $\boldsymbol{E}$, the elastoplastic tangent operator $\boldsymbol{L}_{ep} = \frac{\partial\underset{\sim}{\boldsymbol{\sigma}}}{\partial\underset{\sim}{\boldsymbol{\varepsilon}}}$, or the consistent tangent operator $\boldsymbol{L}_c = \frac{\partial\Delta\underset{\sim}{\boldsymbol{\sigma}}}{\partial\Delta\underset{\sim}{\boldsymbol{\varepsilon}}}$ provided by step (c). This operator is updated for each iteration (classical Newton method), or only for the first or for the first two iterations (modified Newton method).

Step (c) of the Newton–Raphson procedure requires to integrate the elastoviscoplastic constitutive equations at each Gauss point. This integration can be performed using either Runge–Kutta or Θ-method. Using a Runge–Kutta method, the tensor of elastic moduli $\boldsymbol{E}$ is usually chosen for $\boldsymbol{L}$ in the calculation of matrix $\mathbb{K}^i_k$ (see Eq. (2)). The Θ-method requires the calculation of a Jacobian matrix that provides the consistent tangent operator $\boldsymbol{L}_c$. The use of this estimate instead of the tensor of elastic moduli for $\boldsymbol{L}$ in step (f) of the global procedure induces a better global convergence and decreases the number of local iterations for each global calculation increment. However, for the elastoviscoplastic MC model used in this work, the Θ-method can fail to integrate constitutive equations (divergence of the local procedure), in particular when large increments of internal variables occur.

2.2. Constitutive equations

The finite strain formulation for isotropic non-linear material behavior adopted in this work is based on the use of a local objective frame as proposed in [67,11,13]. Observer invariant stress and strain rate measures $\boldsymbol{\sigma}$ and $\dot{\boldsymbol{\varepsilon}}$ are defined by transport of the Cauchy stress $\boldsymbol{T}$ and strain rate $\boldsymbol{D}$ into the corotational frame characterized by the rotation $\underset{\sim}{\boldsymbol{Q}}(\underline{\boldsymbol{x}}, t)$. This change of frame takes place at each material point:

$$\begin{cases} \underset{\sim}{\boldsymbol{\sigma}} = \underset{\sim}{\boldsymbol{Q}}\cdot\underset{\sim}{\mathbf{T}}\cdot\underset{\sim}{\boldsymbol{Q}} \sim T, \\ \dot{\underset{\sim}{\boldsymbol{\varepsilon}}} = \underset{\sim}{\boldsymbol{Q}}\cdot\underset{\sim}{\boldsymbol{D}}\cdot\underset{\sim}{\boldsymbol{Q}} \sim T, \\ \underset{\sim}{\boldsymbol{Q}} \text{ such as } \dot{\underset{\sim}{\boldsymbol{Q}}} \sim T\cdot\underset{\sim}{\boldsymbol{Q}} = \underset{\sim}{\boldsymbol{\Omega}} \text{ (corotational)}, \end{cases} \tag{3}$$

where $\boldsymbol{\Omega}$ is the skew-symmetric part of the gradient $\boldsymbol{L}$ of the velocity field [67,13]. The strain rate tensor $\dot{\boldsymbol{\varepsilon}}$ is split into elastic and plastic contributions, the evolution of the latter being given by the plastic flow rule.

$$\dot{\underset{\sim}{\boldsymbol{\varepsilon}}} = \dot{\underset{\sim}{\boldsymbol{\varepsilon}}}_e + \dot{\underset{\sim}{\boldsymbol{\varepsilon}}}_p, \tag{4}$$

$$\underset{\sim}{\boldsymbol{\sigma}} = \underset{\approx}{\boldsymbol{E}} : \underset{\sim}{\boldsymbol{\varepsilon}}_e, \tag{5}$$

$$f(\underset{\sim}{\boldsymbol{\sigma}}, p, t_a) = J_2(\underset{\sim}{\boldsymbol{\sigma}}) - R(p) - P_1C_s(p, t_a), \tag{6}$$

$$R(p) = R_0 + Q(1 - e^{-bp}), \tag{7}$$

$$\dot{\underset{\sim}{\boldsymbol{\varepsilon}}}_p = \dot{p}\,\underset{\sim}{\boldsymbol{n}}, \tag{8}$$

$$\underset{\sim}{\boldsymbol{n}} = \frac{\partial f}{\partial\underset{\sim}{\boldsymbol{\sigma}}} = \frac{3}{2}\frac{\underset{\sim}{\boldsymbol{s}}}{J_2(\underset{\sim}{\boldsymbol{\sigma}})}, \tag{9}$$

where $J_2(\underset{\sim}{\boldsymbol{\sigma}})$ is the von Mises invariant of the stress tensor, $\boldsymbol{s}$ is the deviatoric part of the stress tensor $\underset{\sim}{\boldsymbol{\sigma}}$, $R(p)$ is the non-linear hardening law, and $P_1C_s(p, t_a)$ is the extra-hardening induced by strain ageing [74,35]. The over-concentration C_s of solute atoms around dislocations is estimated as a function of both internal variables of the model, the cumulated plastic strain p and the ageing time t_a:

$$C_s(p, t_a) = C_m(1 - e^{-P_2p^\alpha t_a^n}). \tag{10}$$

The maximal over-concentration is C_m. P_2 characterizes the rate of saturation of solute atoms around dislocations. Effect of ageing on the flow stress is given by parameter P_1 (units MPa). In fact, only the product P_1C_m can be identified based on mechanical tests. The cumulated plastic strain rate $\dot{p}$ is computed from the following viscoplastic hyperbolic flow rule.

$$\dot{p} = g(f) = \dot{p}_0\sinh\left(\frac{\langle f\rangle}{K}\right), \quad \langle f\rangle = \frac{|f| + f}{2}. \tag{11}$$

The ageing time increment is computed from an evolution law in which the cumulated plastic strain rate $\dot{p}$ intervenes:

$$\dot{t}_a = 1 - \frac{t_a}{w}\dot{p}, \tag{12}$$

where w is the increment of the plastic strain which is produced when all stopped dislocations overcome their obstacles. Such a model has already been used for finite element simulations in [74,35,36,39,24,40,8].

These constitutive equations can be put together in the following form:

$$\dot{\mathbf{Z}} = \mathbf{F}(\mathbf{Z}, \dot{\underset{\sim}{\boldsymbol{\varepsilon}}}), \tag{13}$$

where $\mathbf{Z}$ contains the scalar and tensorial internal/state variables of the model:

$$\mathbf{Z} = (\underset{\sim}{\boldsymbol{\varepsilon}}_e, p, t_a). \tag{14}$$

Eq. (13) can be integrated using either Runge–Kutta or Θ-method.

2.3. Runge–Kutta method

In the Runge–Kutta method, the updated variables at the end of the increment $(t + \Delta t)$ are evaluated from variables and rates of variables at time t. This method relies on Taylor developments of $\mathbf{Z}^{t+\Delta t}$. The first order developments of $\mathbf{Z}^{t+\Delta t}$ gives the Euler method. Function $\mathbf{F}$ in (13) is assumed to be constant and equal to its initial value (i.e. at t) over the whole time increment Δt. This method becomes obviously inaccurate when increasing the global time increment Δt, and consequently the total strain increment $\Delta\boldsymbol{\varepsilon}^t$.

However the method can be improved by a combination of Taylor developments at higher orders, automatic stepping, and error correction. This combination constitutes the Runge–Kutta method of integration [60,70,13]. The global time increment Δt is divided in sub-steps δt_k such as $\Delta t = \sum_k \delta t_k$. The local time step δt_k is controlled by an error correction. In this way, large local time increments are used when $\dot{\mathbf{Z}}$ is rather constant with respect to time, and small ones when $\dot{\mathbf{Z}}$ varies a lot. A development at higher order

of $\mathbf{Z}^{t+\Delta t}$ is also acceptable, if it allows larger sub-steps δt_k for the same precision. In the present work, a fourth order Runge–Kutta method was used. This method provides high confidence in the quality of integration, but can be quite expensive during calculation [13].

2.4. Θ-method

The evaluation of the increment of state variables $\Delta\mathbf{Z}$ according to the Θ-method is performed using unknown values of rate of state variables $\dot{\mathbf{Z}}$ at an intermediate point in the increment:

$$\Delta\mathbf{Z} = \dot{\mathbf{Z}}^{\mathbf{t+\Theta\Delta t}}\Delta t = \mathbf{F}(\mathbf{Z}^{t+\Theta\Delta t}, \underset{\sim}{\Delta\boldsymbol{\varepsilon}}^{t+\Theta\Delta t})\Delta t, \tag{15}$$

$$\mathbf{Z}^{\mathbf{t+\Theta\Delta t}} = \mathbf{Z}^{t} + \Theta\Delta\mathbf{Z}, \tag{16}$$

where $\Theta \in [0;1]$ characterizes the time where variables are evaluated. $\Theta = 0$ corresponds to the Euler scheme, and $\Theta = 1$ to a fully implicit integration. The increment $\Delta\mathbf{Z}$ is then evaluated by solving the following non-linear system with respect to $\Delta\mathbf{Z}$:

$$\mathbf{R} = \Delta\mathbf{Z} - \Delta t\mathbf{F}(\mathbf{Z}^{t} + \Theta\Delta\mathbf{Z}, \underset{\sim}{\Delta\boldsymbol{\varepsilon}}^{t+\Theta\Delta t}) = 0, \tag{17}$$

where $\mathbf{R}$ is called the local residual. In the case of the MC model presented previously the local residual is:

$$\underset{\sim\sim}{\boldsymbol{R}}_{\varepsilon_e} = \Delta\underset{\sim}{\boldsymbol{\varepsilon}}_e + \Delta\underset{\sim}{\boldsymbol{\varepsilon}}_p - \Delta\underset{\sim}{\boldsymbol{\varepsilon}} = \Delta\underset{\sim}{\boldsymbol{\varepsilon}}_e + \Delta p\,\underset{\sim}{\boldsymbol{n}} - \Delta\underset{\sim}{\boldsymbol{\varepsilon}}, \tag{18}$$

$$R_p = \Delta p - g(f)\Delta t, \tag{19}$$

$$R_{t_a} = \Delta t_a - \Delta t + \frac{t_a}{w}\Delta p. \tag{20}$$

A Newton–Raphson algorithm is used to solve the non-linear system. It requires the calculation of the Jacobian matrix associated to system (17).

$$\mathbf{J} = \frac{\partial\mathbf{R}}{\partial\Delta\mathbf{Z}} = \mathbf{1} - \Delta t\frac{\partial\mathbf{F}}{\partial\Delta\mathbf{Z}}\bigg|^{t+\Theta\Delta t}. \tag{21}$$

The Jacobian matrix for the dynamic strain ageing MC model is:

$$\frac{\partial R_{\underset{\sim}{\varepsilon}_e}}{\partial\Delta\mathbf{Z}}\begin{cases}\frac{\partial R_{\underset{\sim}{\varepsilon}_e}}{\partial\Delta\underset{\sim}{\varepsilon}_e} = \underset{\approx}{\boldsymbol{I}} + \Theta\Delta p(\underset{\approx}{\boldsymbol{N}} : \underset{\approx}{\boldsymbol{E}}),\\ \frac{\partial R_{\underset{\sim}{\varepsilon}_e}}{\partial\Delta p} = \underset{\sim}{\boldsymbol{n}},\\ \frac{\partial R_{\underset{\sim}{\varepsilon}_e}}{\partial\Delta t_a} = \underset{\sim}{\mathbf{0}}.\end{cases} \tag{22}$$

$$\frac{\partial R_p}{\partial\Delta\mathbf{Z}}\begin{cases}\frac{\partial R_p}{\partial\Delta\underset{\sim}{\varepsilon}_e} = -\Theta g'(\underset{\approx}{\boldsymbol{N}} : \underset{\approx}{\boldsymbol{E}})\Delta t,\\ \frac{\partial R_p}{\partial\Delta p} = 1 + \Theta g'(H + C_p)\Delta t,\\ \frac{\partial R_p}{\partial\Delta t_a} = \Theta g' C_{t_a}\Delta t.\end{cases} \tag{23}$$

$$\frac{\partial R_{t_a}}{\partial\Delta\mathbf{Z}}\begin{cases}\frac{\partial R_{t_a}}{\partial\Delta\underset{\sim}{\varepsilon}_e} = \underset{\sim}{\mathbf{0}},\\ \frac{\partial R_{t_a}}{\partial\Delta p} = \frac{t_a}{w},\\ \frac{\partial R_{t_a}}{\partial\Delta t_a} = 1 + \Theta\frac{\Delta p}{w}.\end{cases} \tag{24}$$

where $\underset{\sim}{\boldsymbol{n}} = \frac{\partial f}{\partial\underset{\sim}{\boldsymbol{\sigma}}}, \underset{\approx}{\boldsymbol{N}} = \frac{\partial\underset{\sim}{\boldsymbol{n}}}{\partial\underset{\sim}{\boldsymbol{\sigma}}}, \underset{\approx}{\boldsymbol{E}}$ is the fourth order elasticity tensor, $g' = \frac{dg}{df}$, $H = \frac{\partial R}{\partial p}$, $C_p = P_1\frac{\partial C_s}{\partial p}$, $C_{t_a} = P_1\frac{\partial C_s}{\partial t_a}$.

2.5. Proposed t-method and rkt-method

Three numerical methods for the integration of constitutive equations are compared in this work. Two of them (“rkt-method” and “t-method”) are original integration methods based on combination of Runge–Kutta method and Θ-method. The main objective of such combined methods is to avoid local divergence and preserve fast global convergence.

- The first integration method denoted “rk-method” is an explicit fourth order Runge–Kutta method with automatic time stepping, associated with the tensor of elastic moduli $\underset{\approx}{\boldsymbol{E}}$ as an estimate of the actual tangent operator.
- The second method denoted “rkt-method” evaluates the increments of state variables using the Runge–Kutta method at each Gauss point. The consistent tangent operator $\underset{\approx}{\boldsymbol{L}}_c$ is then calculated using the converged variable increments, and used as the estimate of the actual tangent operator.
- The third method denoted “t-method” tries to evaluate the state/internal variable increments using the Θ-method. If the Θ-method fails, increments of variables are evaluated using a fourth order Runge–Kutta method. Then, the consistent tangent operator $\underset{\approx}{\boldsymbol{L}}_c$ is calculated at each Gauss point using the converged variable increments, even if they were calculated using the Runge–Kutta method. The “t-method” therefore corresponds to an automatic switch from Θ-method to a Runge–Kutta method.

2.6. Example – comparison of different methods

In order to compare the three different methods of constitutive equations integration presented in (2.5), the simulation of a plate in tension is performed. All simulations presented in this work have been carried out using the *Z*set finite element program [14,27]. The specimen geometry is a 12.5 mm × 2.5 mm plate, meshed with 2D 8 nodes plane stress elements with reduced integration (4 Gauss points). The material parameters used here are taken from [52] and are recalled in Table 1. They correspond to the Nickel based superalloy Udimet 720. The numerical solution of this problem, solved using the “t-method”, for a constant applied global strain rate equal to 10^{-4} s^{-1} is shown in Fig. 1. The critical plastic strain p_c is defined as the plastic strain for which serrations starts. An analytical value of this critical plastic strain can be obtained from a stability analysis as performed in [52]. The value p_c is indicated on the stress/strain curve. The maps of cumulated plastic strain rate $\dot{p}$ and of ageing time t_a are drawn on the structure for a global applied strain $\varepsilon = 5\%$. In the literature, most of finite element simulations dealing with material instabilities on smooth specimens require numerical tricks such as thickness [40] or material properties variations [15] in order to trigger instabilities. Such defects are useful when a precise location of the band along the specimen is wanted. For propagating bands, there is not such a need so that no defect is introduced in the simulation. In all simulations presented in this work, material instabilities are only triggered by the numerical noise.

Many simulations have been performed on the plate in tension in order to compare these three different methods. The efficiency of all methods is evaluated regarding computation time (CPU time using an AMD Opteron 248 2.2 GHz) for a given precision ratio, for tensile tests up to $\varepsilon = 5\%$. Precision is defined either as the global convergence ratio $\boldsymbol{r}$ (see (2.1)), or by calculating the relative difference between the analytical critical plastic strain p_c^{th} and the corresponding numerical values provided by simulations p_c^{num}. Three different global ratio $\boldsymbol{r}$ have been prescribed in this study: 10^{-4}, 10^{-5}, 10^{-6}. All simulations have been performed at the same prescribed constant strain rate $\dot{\varepsilon} = 10^{-4}$ s^{-1}.

Table 1
Material model parameters identified for a nickel based superalloy, Udimet 720 at 500 °C [51].

Elasticity	Hardening	Viscosity	Ageing
$E = 200$ GPa	$R_0 = 1046$ MPa	$K = 1.55$ MPa	$P_1 C_m = 96$ MPa
$\nu = 0.3$	$Q = 2200$ MPa	$\dot{p}_0 = 10^{-4}$ s^{-1}	$P_2 = 4.1$ s^{-n}
	$b = 1.88$		$\alpha = 0.77$
			$n = 0.33$
			$w = 10^{-4}$

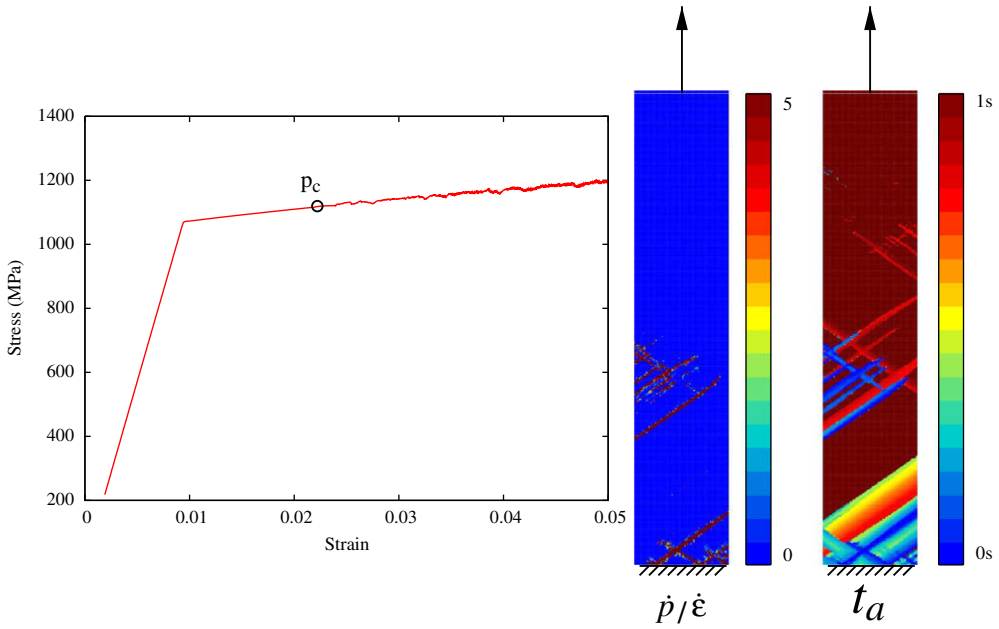

Fig. 1. Numerical solution of a tensile plate made of Udimet 720 at 500 °C. The strain rate is constant and equal to 10^{-4} s^{-1}.

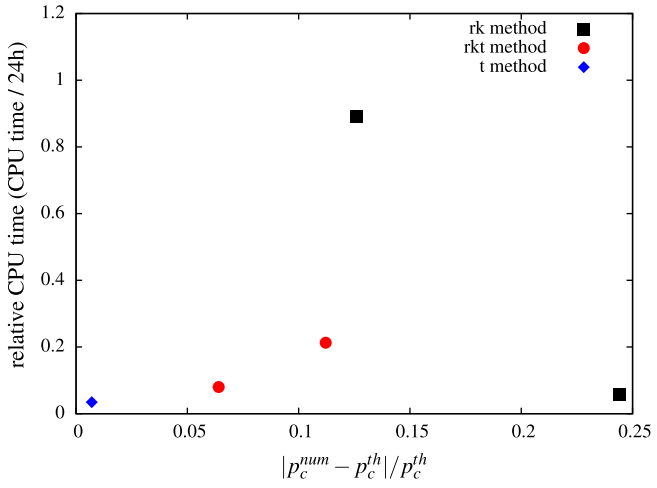

Fig. 2. CPU time length versus relative error on the critical plastic strain for the "rk-method", the "rkt-method", and the "t-method". For all methods the two points correspond to two simulations performed for two different prescribed global convergence ratio $\boldsymbol{r}$ ($\boldsymbol{r} = 10^{-4}$ and $\boldsymbol{r} = 10^{-6}$). For the "t-method", both points coincide.

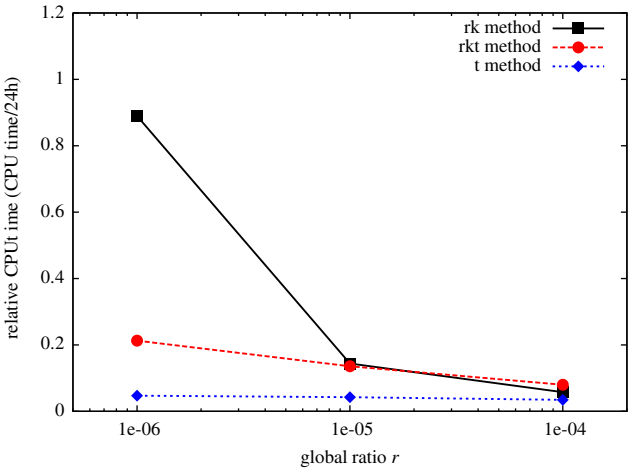

Fig. 3. CPU time length versus prescribed global convergence ratio $\boldsymbol{r}$ for the "rk-method", the "rkt-method", and the "t-method".

On Fig. 2, computation time of simulations for $\boldsymbol{r} = 10^{-4}$ and $\boldsymbol{r} = 10^{-6}$ are plotted with respect to the relative error performed on the critical plastic strain. This error is equal to $|p_c^{num} - p_c^{th}|/p_c^{th}$. Using "rk-method", the precision of the critical plastic strain prediction can be increased prescribing a smaller global ratio, that implies a larger computation time. However this precision remains above 10% even for a one day long simulation. The prediction precision given by the "rkt-method" does not increase with computational time, but remains better for the same CPU time than the "rk-method" one. Finally, the more efficient method is the "t-method" that provides accurate and fast results for both global ratio $\boldsymbol{r}$.

On Fig. 3, the computation time of each simulation is plotted with respect to the prescribed global ratio $\boldsymbol{r}$. The "rk-method" and "rkt-method" lead to similar values for $\boldsymbol{r} = 10^{-4}$ and $\boldsymbol{r} = 10^{-5}$. Indeed, the time earned improving global convergence with the consistent tangent operator $\underset{\approx}{\boldsymbol{L}}_c$ in "rkt-method" is balanced by the time spent for the calculation of this operator. With "rk-method", global convergence is weak but the tensor of elastic moduli $\boldsymbol{E}$ is just calculated once. When $\boldsymbol{r}$ becomes smaller ($\boldsymbol{r} = 10^{-6}$), the global convergence of "rk-method" is so weak that the computation time increases dramatically. On the contrary, because of the consistent tangent operator, the computation time of "rkt-method" keeps increasing as a linear function of the global ratio $\boldsymbol{r}$. With "t-method", the CPU time is almost not affected by a global ratio reduction. One can then get a better precision for almost the same calculation time. From both figures, it is clear that the "t-method" is more efficient than the two other evaluated methods for simulation of the Portevin–Le Chatelier effect using the MC model. A validation on local fields remains to be done.

3. Band nomenclature and band location indicator

In this section, the PLC band nomenclature is reviewed. Then, an original numerical tool that helps to determine the type of bands

that form during finite element simulations is presented. This tool is used to evaluate the strain rate sensitivity of localized phenomena in a plate in tension. Simulations have been performed with constitutive equations of MC model presented in the previous section, and parameters for Udimet 720 at 500 °C given in Table 1.

3.1. Band nomenclature

The localization band type can be described either by the type of serration on the global stress/strain curve [47,48,66], or by the spatio-temporal organization of bands at the surface of specimens [61,50,2,38,20,62]. In the present work, spatio-temporal aspects of localization are mainly considered, but the shape of serration is also sometimes used to confirm the type of bands. Type A and type B bands are associated with propagation along the specimen in the same direction. Type A propagation is continuous while type B bands are characterized by hopping propagation. Type C bands are characterized by random nucleation anywhere in the specimen without propagation. The nomenclature of bands A, B, C is based on ideal pure types, while in most experimental works and finite element analysis one get mostly some behaviors located in the smooth transition domains (denoted here A–B and B–C) existing between two of these pure types.

The spatio-temporal organization of bands can be determined using advanced experimental techniques such as laser extensometry [21,20], or infrared pyrometry [61,62]. Typical results provided by this method are spatio-temporal patterns (STP) given in Figs. 4 and 5. STP describe the location of bands at different stages of experiments, for given spatial and temporal resolutions. These patterns are useful to make the difference between propagating (A–B) and non propagating (B–C) bands. STP associated with propagating bands, at least on the last part of experiments, are given on Fig. 4 for three different types of propagation. Short propagation type is denoted A–B 1, propagation along the whole specimen with reflections at its end is denoted A–B 2, and propagation along the whole specimen with bands nucleating always at the same end is denoted A–B 3. An experimental STP associated with a random nucleated (C type) is presented on Fig. 5. Moreover, the band types are relevant for steady regimes of material deformation. The beginning of the curve corresponds to a transient regime that we call T in the sequel. It cannot be attributed to A–B or C types. Most of experimental and numerical patterns show after this transitory behavior, either A–B or/and B–C types. Indeed, this type of bands detected during experiments depends on strain and strain rate.

At small strain rates, C type bands are mainly observed, while at higher strain rates, A type bands appear. For intermediate strain rates, B type bands are obtained [21,20,61,62].

The evolution of band type with strain level is more controversial. In some articles, band type seems not to vary with strain level for a given prescribed strain rate [50,2,38,1]. But in some others, band type changes for increasing tensile deformation at a given strain rate. The evolutions that can be found in the literature for increasing deformation are A followed by B [20,62], C followed by B [21], B followed by C [61]; and even mixed forms A + B and B + C are observed in [48].

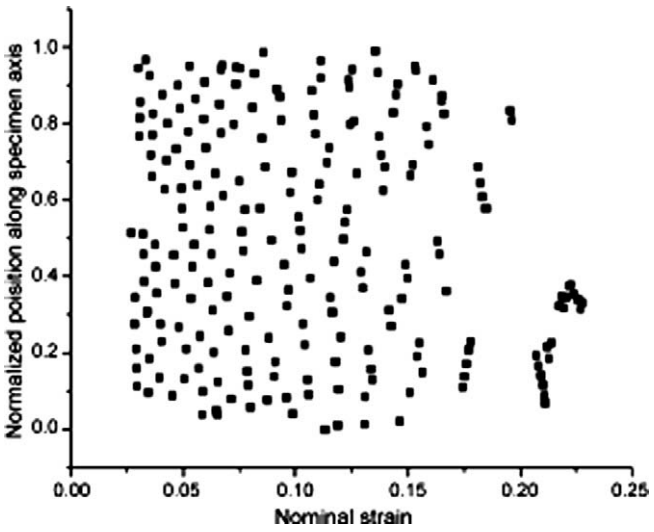

Fig. 5. Spatio-temporal pattern (STP) associated with randomly nucleated bands (type C) [62].

3.2. Numerical detection of bands – the BLI tool

An original numerical method that helps to detect the band propagating behaviors (A–B 1,2,3 or B–C) in a finite element simulation is proposed here. The aim of this method is to mimic, from a numerical point of view, the spatio-temporal patterns (STP) obtained either experimentally in [21,20] using laser extensometry, and in [61,62] using infrared pyrometry, or from theoretical analysis [47,37].

At a given point of the structure, the passing of a band is related to a large value of the plastic strain rate in the zone where it is detected. A simple numerical tool, called Band Location Indicator (BLI), has been implemented in the finite element program *Z*set [14]. At each time step of the non-linear simulation, the program checks at each integration point if the cumulated plastic strain rate $\dot{p}$ is larger than a given value $\dot{p}_1 = \gamma \times \dot{\varepsilon}$ where γ is called the BLI factor and $\dot{\varepsilon}$ is the external strain rate applied on the whole structure. If this condition is fulfilled, i.e. if the integration point is located " inside a localization band ", the program returns the time step value and the axial location y of this integration point. This method of analysis has been tested on a plate in tension at a constant global strain rate equal to 10^{-2} s^{-1} for the nickel based superalloy considered in this work. The 12.5×2.5 mm plate is meshed

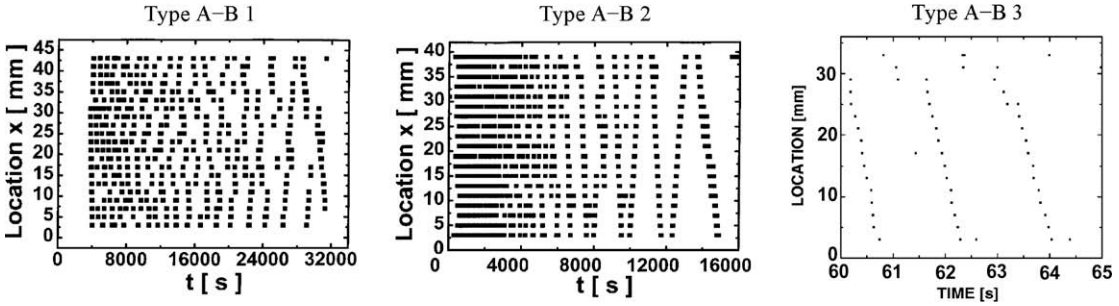

Fig. 4. Spatio-temporal patterns (STP) associated with passing of propagating bands (type A–B), at least on the last part of experiments [21,20].

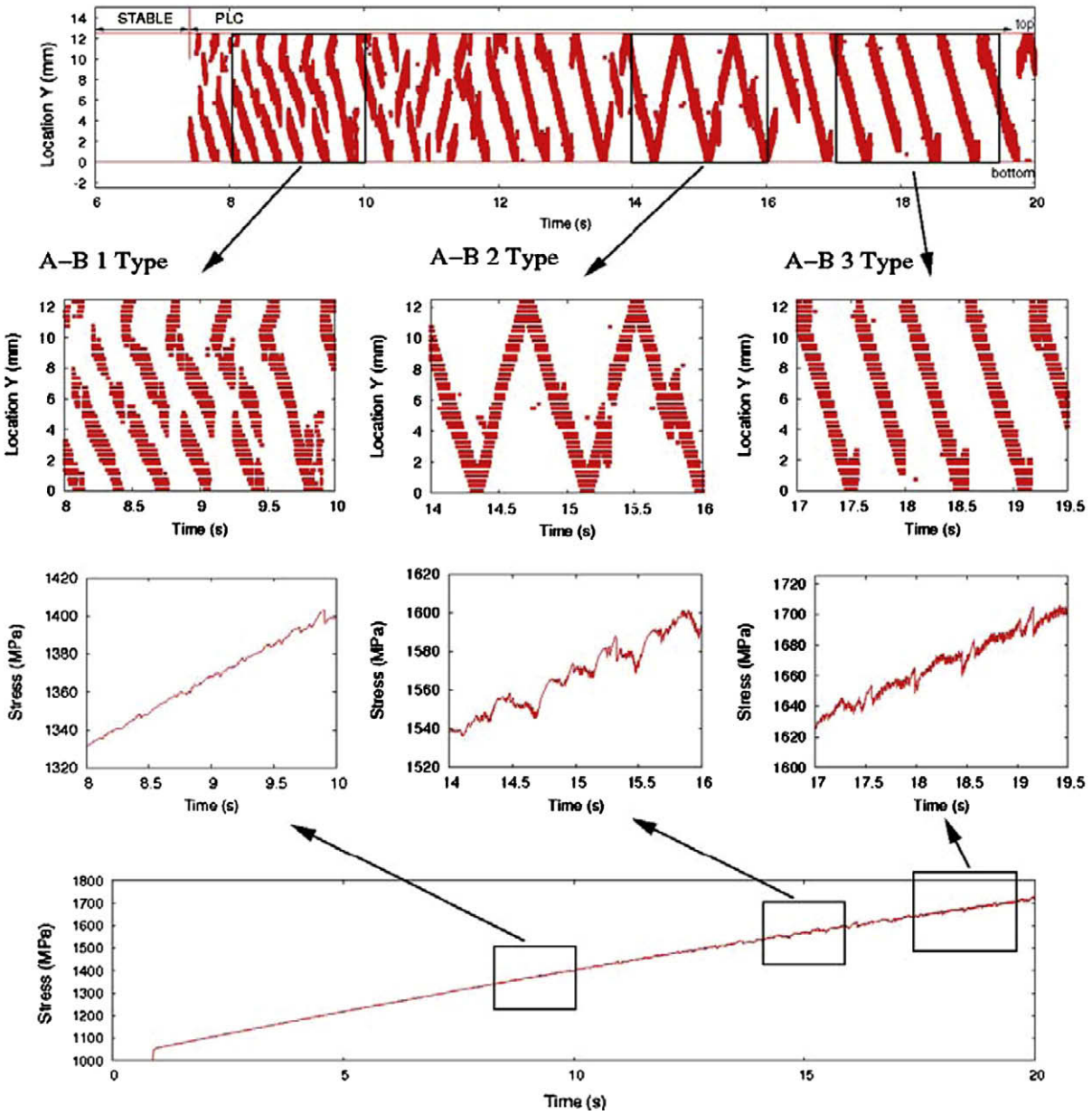

Fig. 6. Simulation of types A–B propagating bands for a plate in tension at a constant strain rate equal to 10^{-2} s^{-1}. First line shows the location of bands as a function of time provided by the Band Location Indicator (BLI). The second line shows three zooms at first line where the three types of propagation appear. Third line contains the corresponding serrations. The fourth line gives the global stress/strain curve of this simulation.

with 80 2D 8 nodes plane stress square elements with reduced integration. The cutting value of the cumulated plastic strain rate for the BLI is $\dot{p}_1 = 5 \times 10^{-2}$ $s^{-1}(\gamma = 5)$. This value of 5 for the BLI factor has been empirically determined from both following observations: A smaller value (close to 1) leads to too many integration points inside bands, a larger value (larger than 10) may exclude all points even though a band actually exists.

Results are outlined in Fig. 6. This simulation reveals the three types of STP associated with propagating types presented on Fig. 4, depending on the overall deformation level. First, for low deformation values, the short propagation A–B 1 type is evidenced. Then for intermediate deformation values, the reflecting at boundary propagation A–B 2 type appears. Finally for high deformation values, the repetitive propagation A–B 3 type is observed. Observing the shape of serrations on the deformation curve, it seems that bands are from A type at the middle of the test and from B type at its end. This point is of particular interest, since a reflecting A–B 2 propagation is sometimes associated with B type bands, while a repetitive A–B 3 propagation appears mostly for A type bands. However, some exceptions to this empirical rule can be found in [21,62] where B type bands are associated with a repetitive A–B 3 propagation.

Even, if it is not the case in this Section, the BLI tool is able to distinguish the continuous propagation of type A from hopping propagation from type B. Hooping propagations can be observed if the time and space resolutions are fine enough to detect discontinuities in the STP, like at the end of this work on Fig. 20.

3.3. Evaluation of band width and velocity from the BLI tool

This method is also accurate to evaluate the width L_b and the velocity V_b of bands. Fig. 7 gives a schematic representation of a

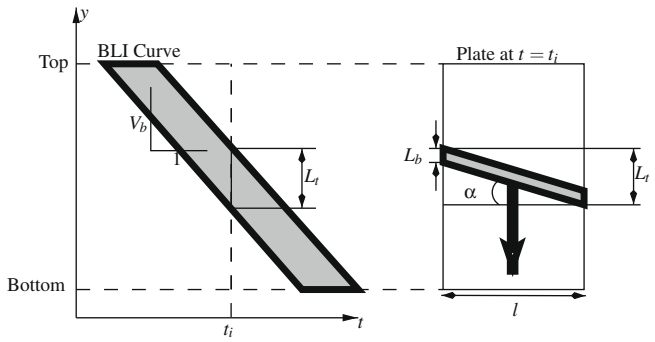

Fig. 7. Measures of band velocity V_b and band width L_b using BLI plot. A schematic BLI plot is drawn on the left and a band in a plate at $t = t_i$ on the right. l denotes the plate width and L_t the width measured on the BLI curve at $t = t_i$. The true width of a band is then $L_b = L_t - l\tan(\alpha)$.

band and its corresponding BLI curve. α denotes the band inclination angle. For all calculations of L_b carried out during 2D analysis (i.e. in Sections 3 and 4), this angle is assumed to be equal to 34.5°. This theoretical value provided by a linear perturbation analysis [7,51] is very close to those found during finite element simulations. l is the current plate width, and the BLI plot width at $t = t_i$ is denoted L_t. The true width of a band is then $L_b = L_t - l\tan(\alpha)$.

The velocity V_b of bands is given by the average slope of BLI plots (see Fig. 7). One can observe on Fig. 6 that this velocity is rather constant during the whole simulation, whatever the band type. This velocity given by the slope of the linear segments of BLI plots, is actually found to decrease slightly with strain in measurements performed by [50,61,62]. The model is perhaps unable to reproduce this effect or the precision of BLI tool is insufficient. The band width is related to the thickness of curves and consequently to the BLI factor γ. Since the BLI detects points in the whole

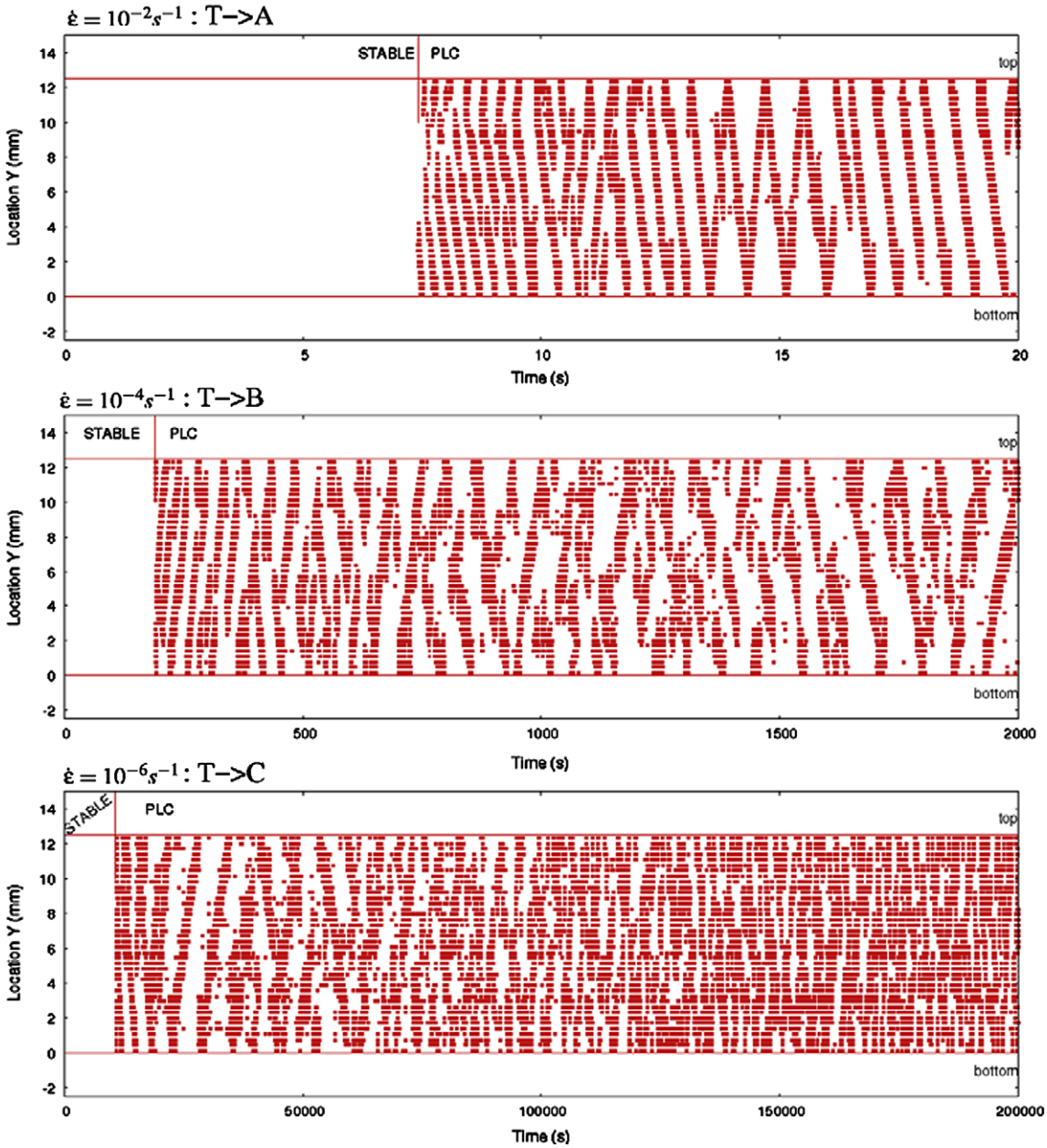

Fig. 8. Spatio-temporal patterns along a plate in tension for three different prescribed strain rates.

width of specimens, the inclination of bands have to be taken into account to calculate the true width of bands (see Fig. 7).

3.4. Application: strain rate sensitivity

The BLI is useful to compare different simulations at different global applied strain rates. On Fig. 8, band location is plotted as a function of time for three different strain rates: 10^{-2} s^{-1}, 10^{-4} s^{-1}, 10^{-6} s^{-1}. Simulations have been performed on the same mesh. The corresponding global stress/time curves are plotted on Fig. 9. The critical plastic strain, serrations, and type of bands are highly sensitive to strain rate.

The type of bands is determined from spatio-temporal patterns (STP) associated with observation of serration shapes. For all three simulations a transitory (T) behavior is firstly observed. Then, for higher strain rates (10^{-2} s^{-1} and 10^{-4} s^{-1}), propagating bands are found, while for the lower one (10^{-6} s^{-1}), randomly nucleated bands appear. Observing the shape of serrations of the deformation curve, it seems that C type bands appear for the lower strain rate (10^{-6} s^{-1}), B type bands appear for the intermediate strain rate (10^{-4} s^{-1}), and A type bands appear for the higher strain rate (10^{-2} s^{-1}). These results are in good agreement with experimental observations made in [21,20] on a different material. Another finding is that the critical plastic strain decreases when the strain rate decreases as in [51]. That is not the case in some other works [21,24], but some other prescribed strain rate should be investigated to confirm this monotonous behavior. The frequency (with respect to global strain) and amplitude of serrations on the tensile curve increase, evolving from type A to type C as in [24].

The influence of strain rate on the velocity of bands V_b, and on the amount of plastic strain rate carried by the band Δp are investigated. Are V_b and Δp intrinsic properties of the model parameters or are they functions of global strain rate $\dot{\varepsilon}$? Some measures of the band velocity V_b presented Table 2 have been obtained from Fig. 8 for $\dot{\varepsilon} = 10^{-2}$ s^{-1}, $\dot{\varepsilon} = 10^{-4}$ s^{-1}, $\dot{\varepsilon} = 10^{-6}$ s^{-1}. The average amount of plastic strain rate Δp carried by a band is also measured for the three prescribed strain rates. This quantity is estimated at an integration point at the center of the plate, measuring height of

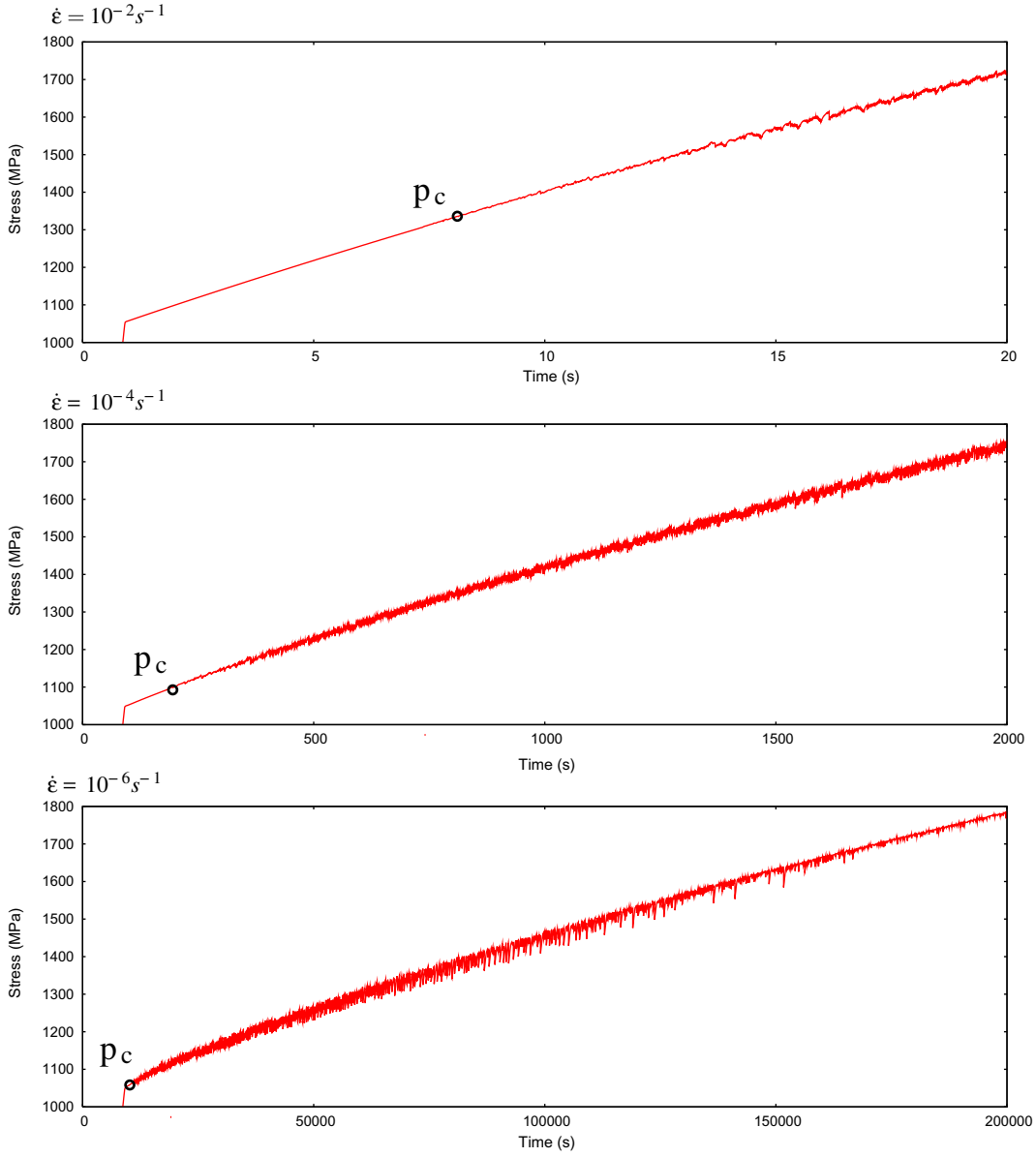

Fig. 9. Global engineering stress vs. time curve for a plate in tension for three different prescribed strain rates.

Table 2
Estimates of the velocity (V_b), and of the average plastic increment carried by the band (Δp), for different prescribed strain rates at $\varepsilon = 17\%$.

Prescribed strain rate $\dot{\varepsilon}$ (s^{-1})	V_b (mm s^{-1})	Δp
10^{-2}	35	0.005
10^{-4}	3.5	0.005
10^{-6}	0.35	0.005

steps on the temporal plastic strain evolution at this point. On the one hand, the velocity seems to be linearly related to the prescribed strain rate. The amount of plastic strain rate appears to be an intrinsic property of the model, since at 17%, Δp is identical for the three strain rates, even if it varies between 0.003 and 0.007 during simulations. for any prescribed strain rate, any strain level, and any mesh (see Section 4). Experimental results on the variation of Δp with strain and strain rate differ. In [62], Δp is mainly related with the nominal strain and does not actually depend on the prescribed strain rate. On the contrary in [50], Δp is found to increase with the nominal strain for A type bands but is quite constant for B types ones. The influence of prescribed strain rate on band kinematics characteristics is also investigated using a theoretical approach in [37]. The band velocity V_b is found to increase with respect to strain rate, like in this work. The band plastic strain Δp also increases, which follows some experimental trends [50], but differs from finite element results presented here or from some other experimental trends [62].

4. Mesh sensitivity of PLC localization phenomena

A mesh sensitivity analysis of the MC model is performed considering the effect of the element size on the global load/displacement curve and the characteristics of localization bands. Six different meshes of a 12.5×2.5 mm plate have been used, the number of degrees of freedom (DOF) varies from 250 to 116354. The simulation of a tensile test has been performed for each mesh using the same material parameters, at two prescribed strain rates equal to 10^{-2} s^{-1} and 10^{-4} s^{-1}. Serrations and the type and shape of bands are first studied from a qualitative point of view. Some characteristic parameters of A-B type bands appearing for 10^{-2} s^{-1} simulations are then evaluated for each mesh, to provide a quantitative analysis of the mesh sensitivity of the MC model.

4.1. Qualitative analysis

4.1.1. Serrations

An homogeneous solution for a uniaxial tensile load can be calculated for the MC model assuming that $\dot{p}$ remains constant [52]:

$$\sigma^{Homogeneous} = K \operatorname{arcsinh}\left(\frac{\dot{p}}{\dot{p}_0}\right) + R_0 + Q(1 - e^{-bp}) + P_1 C_m \left(1 - e^{-P_2 p^{\alpha} t_a^n}\right). \tag{25}$$

The corresponding finite element solution coincides with this solution before the critical plastic strain, and oscillates around it after when serrations begin (see Fig. 1).

The difference between the average stress for different mesh densities and the corresponding analytical homogeneous solution is plotted on Fig. 10 as a function of the cumulated plastic strain p:

$$\Delta\sigma = \frac{F}{S} - \sigma^{Homogeneous}. \tag{26}$$

The critical plastic strain does not significantly depend on mesh size. The shape of serrations seems also to be rather mesh independent. The frequency and the amplitude of oscillations are about the same for all meshes, but solutions do not coincide. The reasons for these differences lie in the impact of the mesh density on the detailed behavior of bands. This behavior can be observed with the band location indicator (BLI) presented in Section 3.2 to locate the position of bands at each step of the simulations.

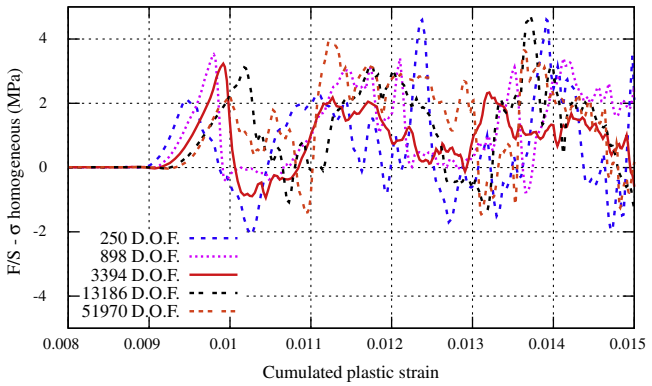

Fig. 10. Numerical global serrated stress minus homogeneous stress $\left(\frac{F}{S} - \sigma^{Homogeneous}\right)$ for a tensile plate at a constant strain rate of 10^{-4} s^{-1}. Simulations have been performed for five different meshes, for the same boundary value problem and material parameters.

The same analysis has been performed at a constant stress rate for five different meshes (cf. Fig. 11). Typical steps are observed on the overall curves, as reported in experiments for steel in [69]. The critical strain for which the typical steps appear remains mesh independent. For a given level of the nominal strain, the plastic strain carried in each band seems to be also mesh independent since the shape of steps does not depend on the mesh size. The difference between each curve is due to a difference in the shape and location of bands as for simulations at a constant strain rate.

4.1.2. Band location

The spatio-temporal patterns (STP) provided by the BLI are given on Fig. 12 for four different meshes. One can first observe that the STP spatial resolution is mesh dependent, but this aspect does not actually affect the determination of propagation type, neither the measuring process of band kinematic properties. For each STP, propagating behaviors associated with A–B bands are observed after the transition behavior. However, the propagation type (A–B 1, A–B 2, A–B 3, see Section 3.2) is found to be mesh dependent. This the propagation type seems to be A–B 31 (type 3 then 1) for the coarse mesh (250 DOF), A–B 123 for the reference one (898 DOF) used for the strain rate sensitivity analysis, A–B 13 for the fine one (3394 DOF), and A–B 131 for the very fine one (13186 DOF). The quantitative analysis of kinematic parameters of such bands developed in the next section will provide further information about mesh sensitivity of bands. Indeed, looking

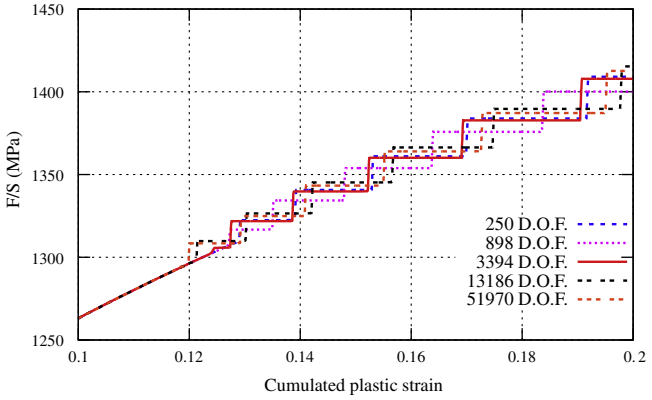

Fig. 11. Numerical global serrated stress for a tensile plate at a constant stress rate. Simulations have been performed for five different meshes, for the same boundary value problem and material parameters.

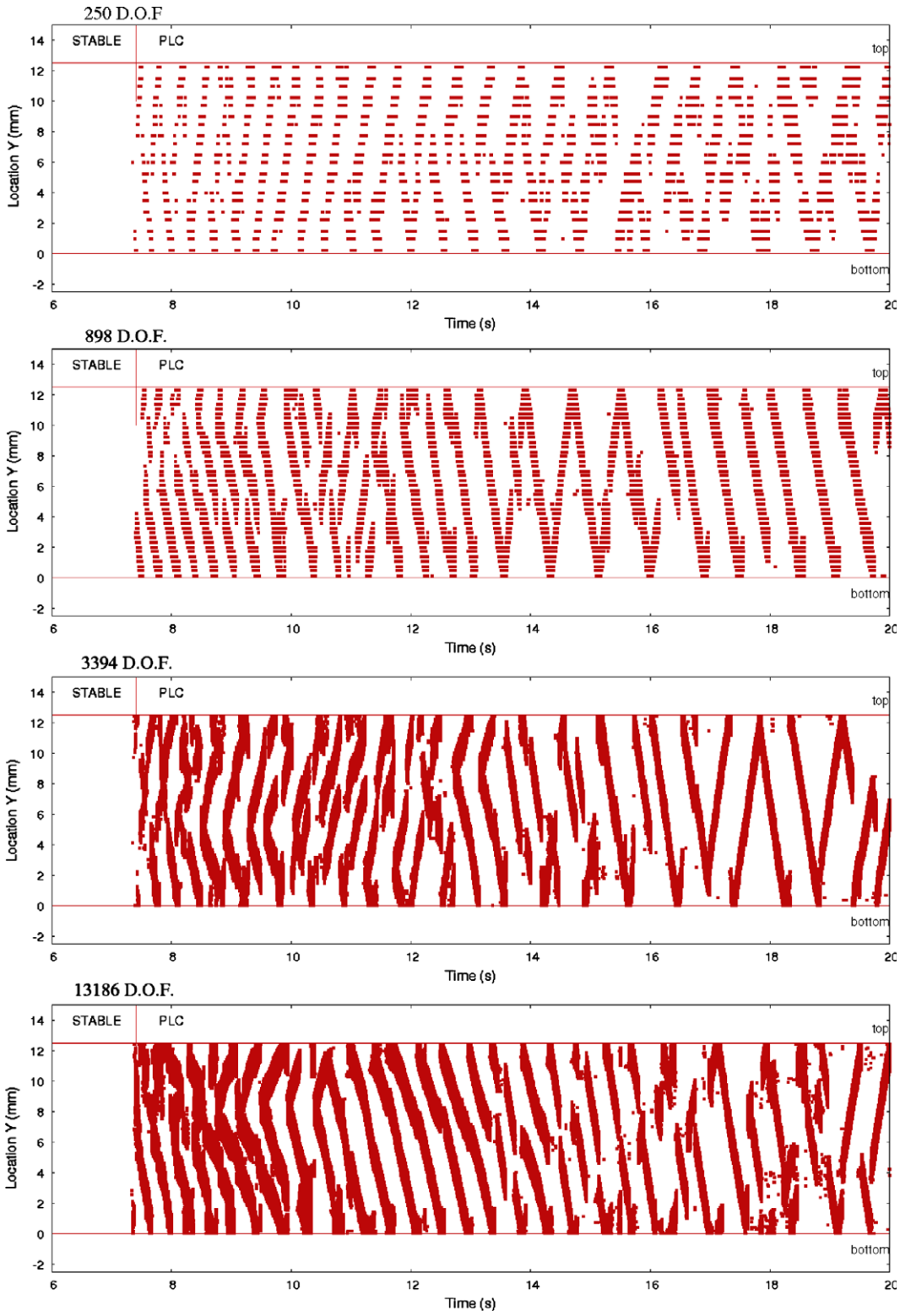

Fig. 12. Spatio-temporal patterns (STP) of bands for a plate in tension for four different mesh densities at a constant strain rate of 10^{-2} s^{-1}.

at STP, the velocity of such bands appears for example to be mesh independent.

4.1.3. Band shapes

The distribution of bands on the sample surface is represented for the four different meshes in Fig. 13. The cumulated plastic strain rate $\dot{p}$ and the ageing time t_a are drawn for the same deformation value. The total strain is $\varepsilon = 9\%$. When the mesh is refined, the number of bands increases and the band width decreases, while the maximum plastic strain increases.

4.2. Quantitative analysis

The quantitative analysis of the mesh sensitivity performed here is based on the measure of kinematic parameters of a single propagating band (type A–B 2 or 3). This analysis is carried out

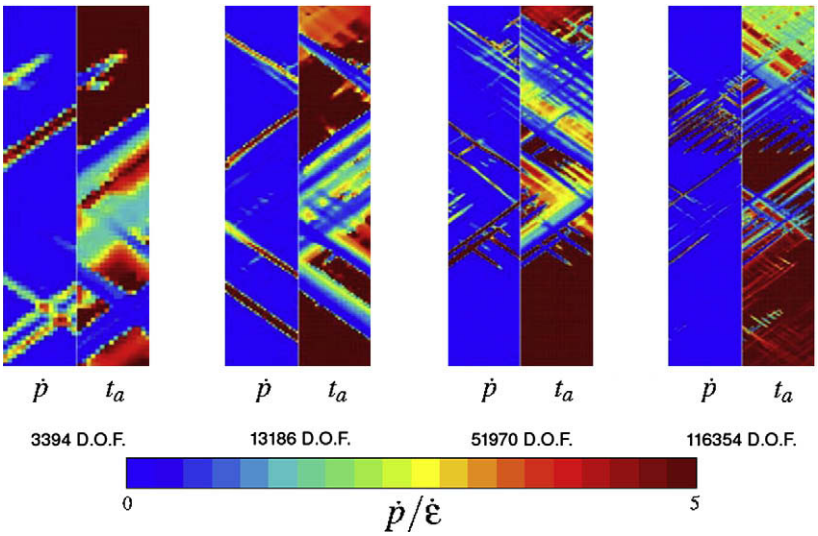

Fig. 13. Cumulated plastic strain rate and ageing time for four meshes for a plate in tension at a constant strain rate $\dot{\varepsilon} = 10^{-2}$ s^{-1}, and for a global strain of $\varepsilon = 9\%(t = 9s)$.

for simulations of plates in tension at a constant strain rate $\dot{\varepsilon} = 10^{-2}$ s^{-1}. The amount of plastic strain carried by the band is $\Delta p = p_2 - p_1$, where p_1 is the plastic strain before the band passing and p_2 after it. The maximal value of the plastic strain rate in the band is denoted $\dot{p}_{max}$. All these kinematics parameters are schematically shown in Fig. 14.

Neglecting the elastic strain rate contribution, a relation between the global prescribed strain rate $\dot{\varepsilon}$, the maximum strain rate in the band $\dot{p}_{max}$, the band width L_b, and the total length of the plate L can be derived [33,2]:

$$\dot{\varepsilon} \approx \langle \dot{p} \rangle = \frac{L_b}{L} \frac{1}{2} \dot{p}_{max}. \tag{27}$$

This relation actually holds for a band with a triangular shape, but can be extended to bands with a different shape changing the expression of the average of $\dot{p}$ along the plate $\langle \dot{p} \rangle$. We propose another relation between the global prescribed strain rate $\dot{\varepsilon}$, the time for the band to propagate from one edge of the specimen to the other Δt, the amount of plastic strain carried by the band is Δp, and the total length of the plate L:

$$\dot{\varepsilon} \approx \frac{\Delta p}{\Delta t} = \frac{\Delta p V_b}{L}. \tag{28}$$

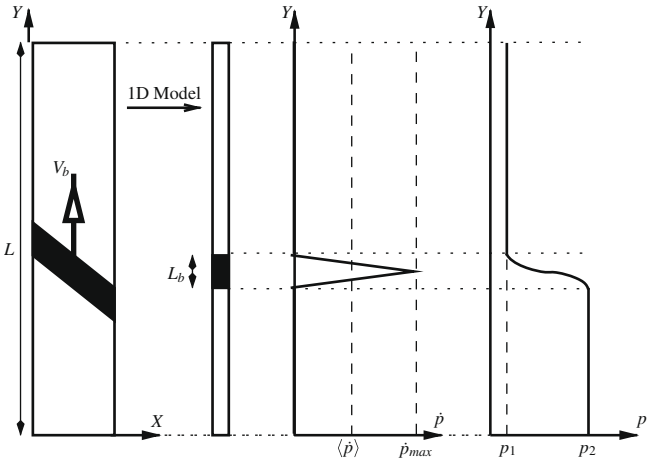

Fig. 14. Kinematic simplified model of a band, based on numerical results.

Then

$$\Rightarrow \Delta p V_b \approx \frac{1}{2} L_b \dot{p}_{max} \approx L\dot{\varepsilon}, \tag{29}$$

where $L\dot{\varepsilon}$ is the prescribed displacement rate. Neglecting the elastic strain rate, this quantity is equivalent to the permanent plastic elongation rate associated with the passing of a single band.

Numerical measurements of the kinematic parameters of bands have been performed for the 6 meshes, for a single propagating band (type A–B 2 or 3) after the initial transition behavior has disappeared. The prescribed strain rate is 10^{-2} s^{-1} and the global strain $\varepsilon = 17\%(t = 17$ s), in a range of deformation where single bands are propagating for all meshes. Results are presented in Table 3 and in Fig. 15.

On Fig. 15, the element sizes are normalized by the value for minimum element size (0.052 mm for 116354 DOF). Parameters are also normalized by their value for the minimum element size. Then the plotted values are normalized by the corresponding value obtained for mesh with 116354 DOF. The amount of plastic strain Δp and the velocity of bands V_b are found to be mesh independent. The band width L_b and the inverse of the maximum plastic strain rate $(\dot{p}_{max})^{-1}$ are linear function of mesh size.

The evolutions of Δp, $(\dot{p}_{max})^{-1}$, and V_b with respect to mesh density is less regular than L_b ones. This imperfection in numerical results arises from the fact that $(\dot{p}_{max})^{-1}$ is actually not constant in a band during the whole propagation from one edge to the other. Moreover, values measured for $(\dot{p}_{max})^{-1}$ and Δp are affected by the presence of the edges of the plate. However, even with such rough measures for Δp and $(\dot{p}_{max})^{-1}$, the relation (29) can be verified. In the case of the finest mesh, we get $\Delta p V_b = 0.149$ mm/s and $1/2 L_b \dot{p}_{max} = 0.138$ mm/s, while $L\dot{\varepsilon} = 0.125$ mm/s. These

Table 3
Estimates of the band velocity (V_b) and band width (L_b), of the plastic increment carried by the band (Δp), of the maximum plastic strain rate $(\dot{p}_{max})$ for different meshes.

Element size (mm)	DOF	V_b (mm s^{-1})	L_b (mm)	Δp	$\dot{p}_{max}$ (s^{-1})
1.25	250	0.398	1.635	0.0038	0.13
0.625	898	0.358	0.808	0.004	0.21
0.3125	3394	0.313	0.388	0.0039	0.54
0.15625	13,186	0.305	0.212	0.0057	0.85
0.078125	51,970	0.284	0.10	0.0052	1.8
0.05208	116,354	0.254	0.0737	0.0059	3.75

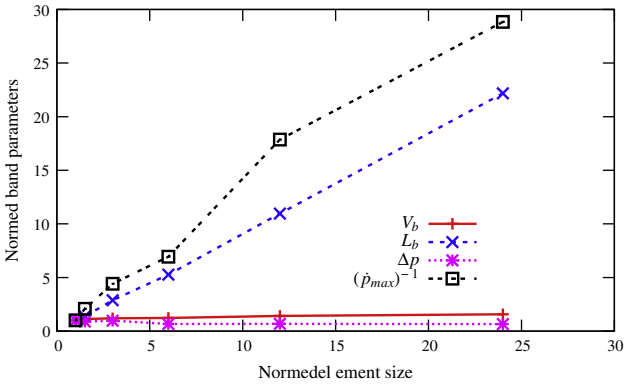

Fig. 15. Evolution of the band velocity (V_b) and band width (L_b), of the plastic increment carried by the band (Δp), of the maximum plastic strain rate ($\dot{p}_{max}$) for different element sizes. Values are normalized with respect to values at the minimum element size. DOF number goes from 250 to 116354.

quantities are rather constant for all different mesh densities. This relation was also checked for different prescribed velocities.

A parallel can be drawn between the propagation of bands of plastic deformation and wall painting. The band width L_b is equivalent to the number of hair in the brush (proportional to the width of the brush), the amount of plastic strain Δp to the quantity of paint spread out per hair per coat, the maximum plastic strain rate $\dot{p}_{max}$ to the quantity of paint laid per second per hair, and the rate of plastic elongation $\int \dot{p} dy \approx L\dot{\varepsilon}$ to the flux of paint between the paintbrush and the wall. The band velocity V_b is equivalent to the apparent axial brush velocity. After each run the brush moves across the

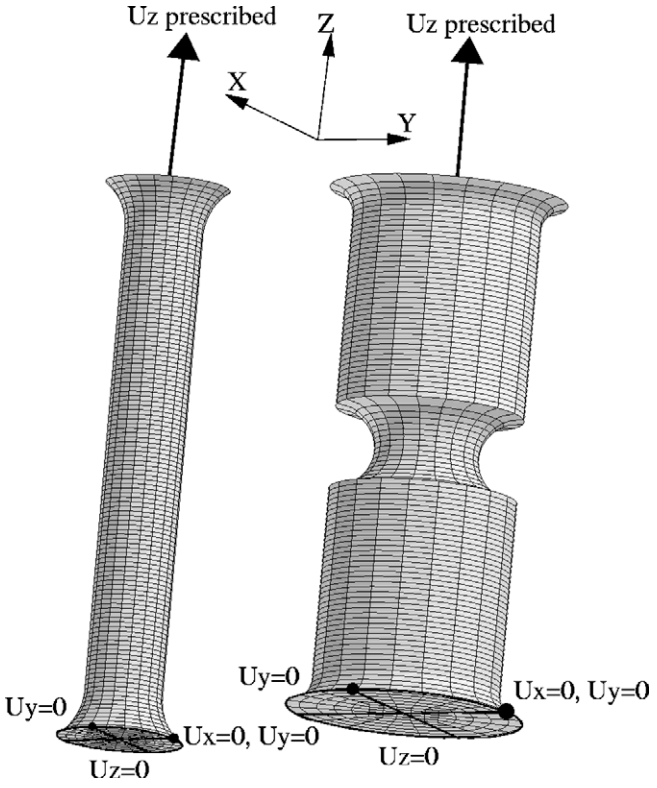

Fig. 16. Mesh and boundary conditions of smooth and notched (NT4) axisymmetric specimens.

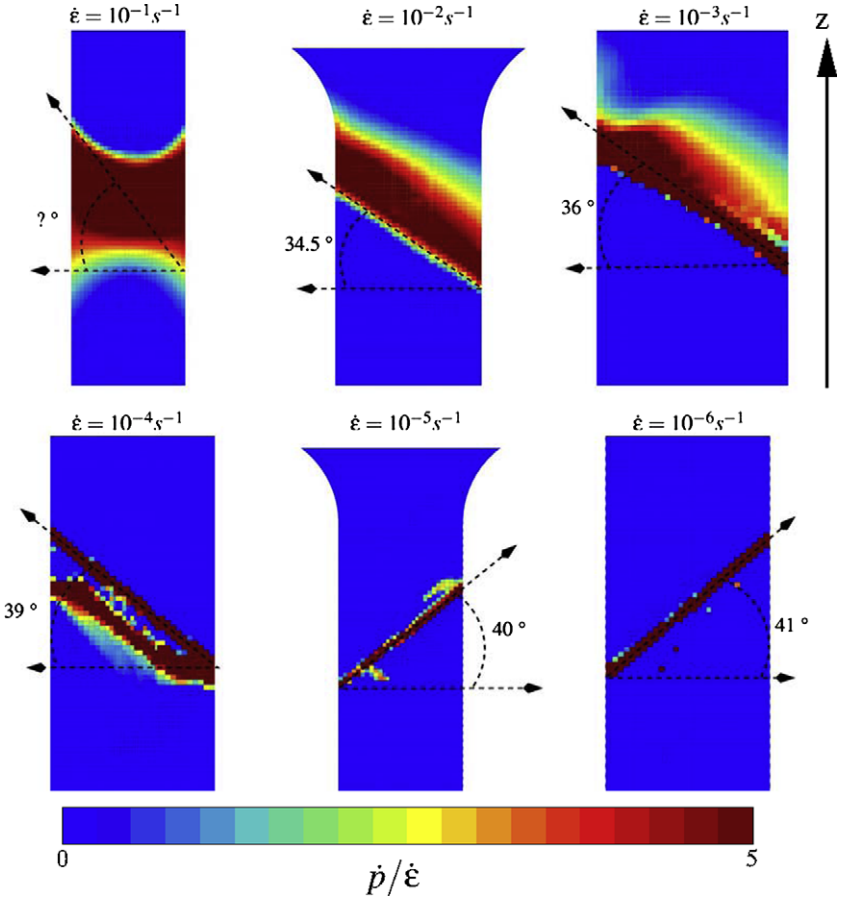

Fig. 17. Orientation and shape of bands for different strain rates in a smooth axisymmetric specimen. Bands are plotted on the central cross-section.

specimen in the axial direction to paint a new strip. A move of several hairs is equivalent to A type bands, while B type bands would be equivalent to a displacement of at least the size of the brush. The effect of a mesh refinement is like using a smaller brush (with less hair on it), and pressing stronger on it to increase the flux per hair, the axial speed of the brush and paint quantity in a coat yet remain the same. During the propagation of a band of plastic strain rate (respectively, in wall painting), whatever the mesh (respectively, brush) size, the rate of plastic elongation (respectively, the flux of paint) remains constant. Then, depending on which quantities need to be accurately reproduced, the mesh will have to be refined or not.

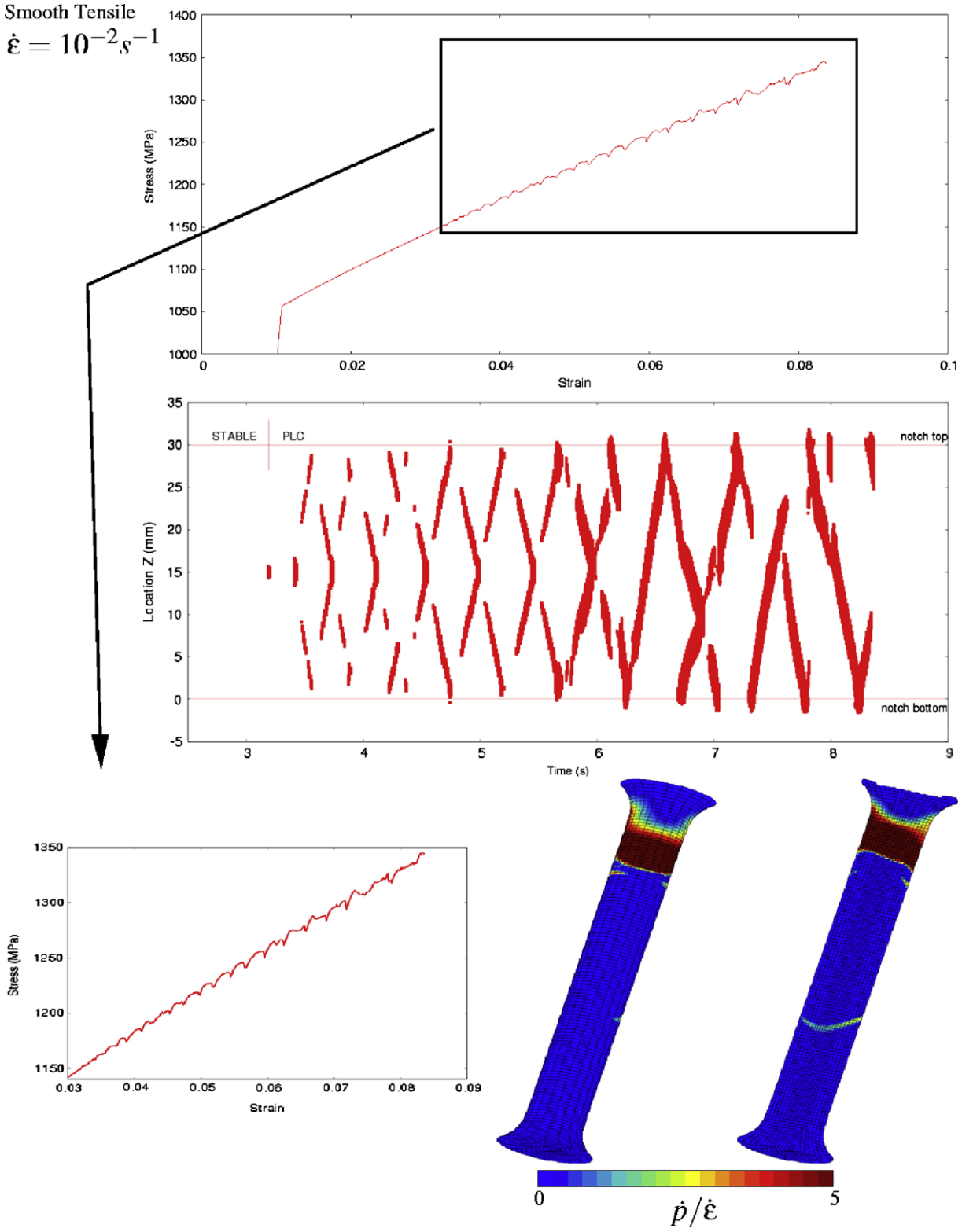

Fig. 18. Global engineering stress/strain curve, location of bands as a function of time, zoom on serrations and plastic strain rate in the specimen at $\varepsilon = 8.25\%$ for a smooth axisymmetric specimen at a prescribed strain rate $\dot{\varepsilon} = 10^{-2}$ s^{-1}.

The MC model presented in this article is efficient to simulate, irrespective of the mesh size, the global behavior, the strain carried in the band, and the band velocity. If one needs to simulate the maximum of plastic strain rate or the band width, a non-local or dynamic model may well be necessary.

5. Smooth and notched 3D tensile specimens

5.1. Numerical models

In the literature, most finite element simulations of the PLC effect have been performed on 2D geometries [71,35,36,24,40]. 2D

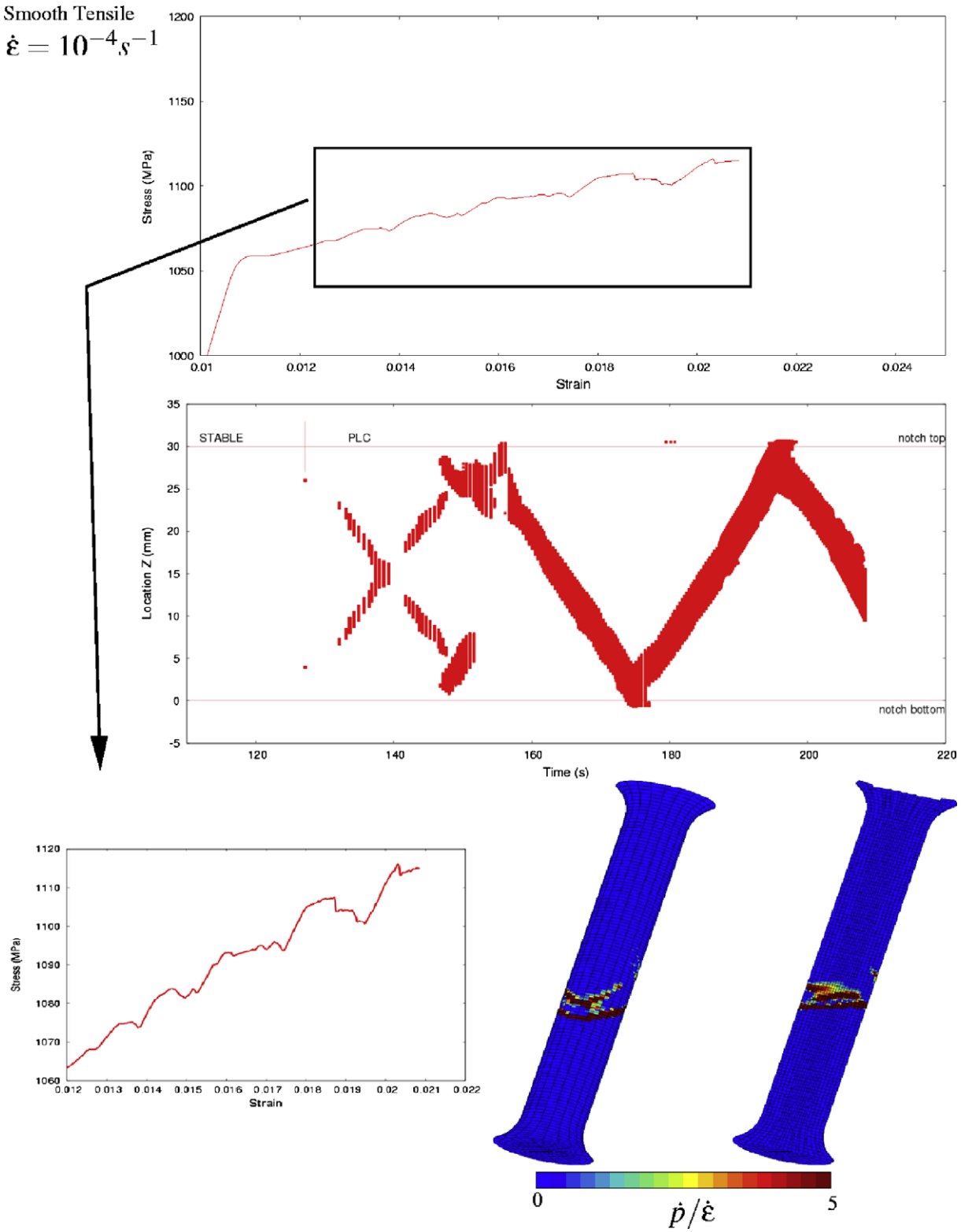

Fig. 19. Global engineering stress/strain curve, location of bands as a function of time, zoom on serrations and plastic strain rate in the specimen at $\varepsilon = 2\%$ for a smooth axisymmetric specimen at a prescribed strain rate $\dot{\varepsilon} = 10^{-4}$ s^{-1}.

axisymmetric meshes have been used by [7] on smooth and notched tensile specimens. The maximum number of degrees of freedom (DOF) for these simulations is 27,960 for smooth tensile (ST) specimens and 9618 for notched tensile (NT) specimens, with one-point integration elements. Simulation with 3D meshes can be found in [74] on smooth flat and axisymmetric specimens, with respectively 7783 and 7011 DOF and 8 nodes incompatible mode elements. In [43], simulations of 3D flat specimens are performed with 5970 DOF using a model for polycrystalline plasticity. Finally, in [39], simulations of 3D smooth tensile specimens are performed with 81,855 DOF and one-point integration elements, like in [8] with almost 75,000 DOF.

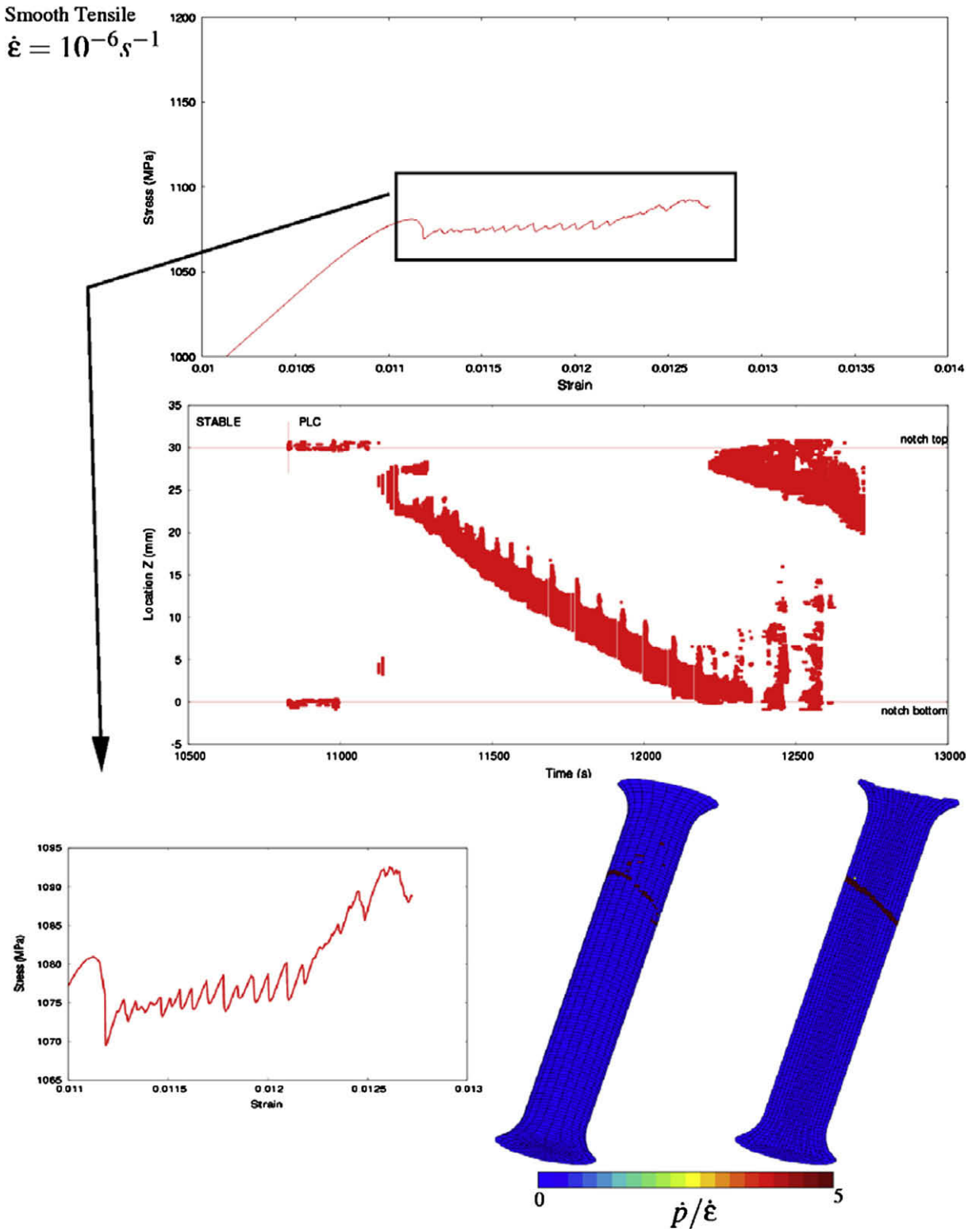

Fig. 20. Global engineering stress/strain curve, location of bands as a function of time, zoom on serrations and plastic strain rate in the specimen at $\varepsilon = 1.26\%$ for a smooth axisymmetric specimen at a prescribed strain rate $\dot{\varepsilon} = 10^{-6}$ s^{-1}.

Table 4
Angle between the tensile axis and the band normal, maximal amplitude of serration, critical plastic strain, and celerity of bands for the six different applied strain rates.

Strain rate	10^{-6} s^{-1}	10^{-5} s^{-1}	10^{-4} s^{-1}	10^{-3} s^{-1}	10^{-2} s^{-1}	10^{-1} s^{-1}
Orientation of bands (°)	41	40	39	36	34.5	–
Maximum amplitude of serrations (MPa)	–	15	12	10	10	8
Critical plastic strain p_c (%)	–	–	0.18	.81	2.2	6.2
Band velocity V_b(mm s^{-1})	0.023	0.15	1.3	8.5	80	790

The objective of this last section is to show the robustness of the proposed numerical approach for 3D finite elements computations. For that purpose, 3D fine meshes of a smooth and a notched tensile specimen have been drawn. Both meshes are built-up from 20-nodes brick elements with reduced integration. The gauge part of the smooth tensile specimen is 30 mm long with a diameter equal to 5 mm. The diameter of the notched tensile specimen is 6 mm in the ligament and 10.8 mm out of the notch. The notch radius is 2.4 mm. Simulations have been performed using a total number of 192,708 DOF for the smooth specimen, and 160,788 DOF for the notched one. Indeed, fine meshes are necessary to determine the type of bands using the BLI. Theses meshes are drawn in Fig. 16 together with the boundary conditions used for simulations.

Finite element simulations have been performed on smooth axisymmetric specimens in order to validate the following trends deduced from experimental results [51]: when the prescribed strain rate decreases, (i) the critical strain decreases, (ii) the frequency of oscillations increases, (iii) the amplitude of oscillations increases. The material model parameter α has been slightly decreased from 0.77 to 0.55 in order to fit more accurately the experimental critical plastic strain [52]. The other parameters remain the same as in Table 1. Six different prescribed strain rates have been simulated ($\dot{\varepsilon} = 10^{-6}$ s^{-1} to $\dot{\varepsilon} = 10^{-1}$ s^{-1}). The effect of the machine stiffness is not taken into account in this work. Band type and orientation with respect to the prescribed strain rate have also been determined.

5.2. Band orientation: symmetry breaking in axisymmetric test samples

Simulations of axisymmetric specimens have been performed by [7] using 2D axisymmetric meshes and by [74,39,8] using 3D meshes. In these studies, bands have generally a conical shape. Sometimes two intersecting bands are observed [39]. To our knowledge there is no simulation available in literature with a full symmetry breaking of band pattern in axisymmetric samples, i.e. a single band propagating like in plates in tension. For small strain rates (below 10^{-4} s^{-1}), this phenomenon has been observed during simulations of smooth axisymmetric specimens.

Angles between band normal and tensile direction have been measured for all simulations. Results of these measures are plotted in Fig. 17. They are found to be equal to the angle predicted form a bifurcation analysis for a purely plastic material, that is close to 42° [64,10].

This value is accurately recovered for $\dot{\varepsilon} = 10^{-6}$ s^{-1} and $\dot{\varepsilon} = 10^{-5}$ s^{-1}, when a single band propagates in the structure. But as soon as twin bands propagate ($\dot{\varepsilon} = 10^{-4}$ s^{-1} and $\dot{\varepsilon} = 10^{-3}$ s^{-1}), this value decreases and seems to tend towards 35° ($\dot{\varepsilon} = 10^{-2}$ s^{-1}), which is the theoretical angle value for a bi-dimensional simple tension. Finally when $\dot{\varepsilon} = 10^{-1}$ s^{-1} no direction can be evaluated because a infinite number of bands are propagating together forming a conical shape. The same type of shape has been observed in [7] on 2D axisymmetric models.

One shall wonder if the orientation of such bands is directly related to the strain rate, or if the angle varies because of band shapes. The explanation proposed in this work is that when the material tends to a purely plastic behavior (for lower strain rates), the model gives less diffuse deformation bands that tend to localize within a unique axial but also radial orientation. Axisymmetry of bands is broken. The theoretical orientation of localization for a tri-dimensional simple tension is valid (42°). For higher strain rates viscosity stabilizes the solution which tends then to localize only with a given axial orientation but with no preferential radial position. Then several bands are propagating together, rotating around the tensile axis. The orientation of bands is deviated and the angle with respect to the tensile axis is reduced. This hypothesis has to be validated for other materials.

5.3. Band type and serration shape

The critical plastic strain for each simulation is evaluated in this section. Frequencies (with respect to global strain) and amplitude of serrations are compared between different prescribed strain

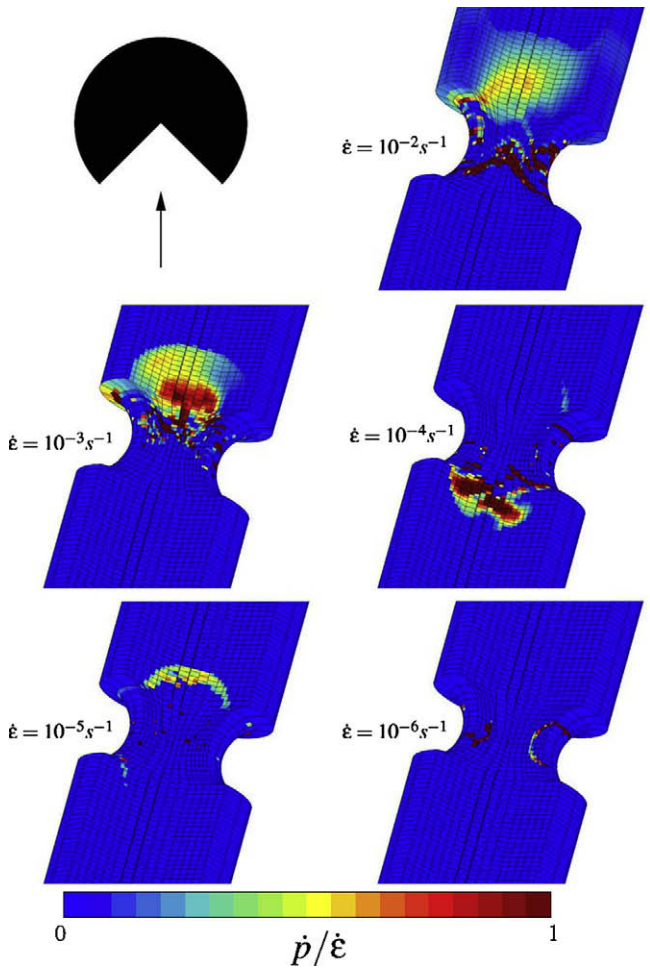

Fig. 21. Shape of bands inside a notched axisymmetric specimen for different strain rates.

rates. Finally the band type for each simulation is determined using the band location indicator.

The numerical critical plastic strain in simulations is provided from a global stability criterion as in [53]. The maximum amplitudes $(2 \times \mathrm{Max}|\frac{F}{S} - \sigma^{Homogeneous}|)$ of serrations for different strain rates are taken from plots of the average stress minus the corresponding analytic homogeneous solution, as in Fig. 10. Finally, measurements of the band velocity are made on the graphs of band location plotted for example in Figs. 18–20. The results of these measurements are summarized in Table 4. When the prescribed strain rate increases, the orientation changes (see Section 5.2), the average frequency (with respect to global strain) and the maximum amplitude decrease, the critical plastic strain increases, the velocity of bands increases linearly.

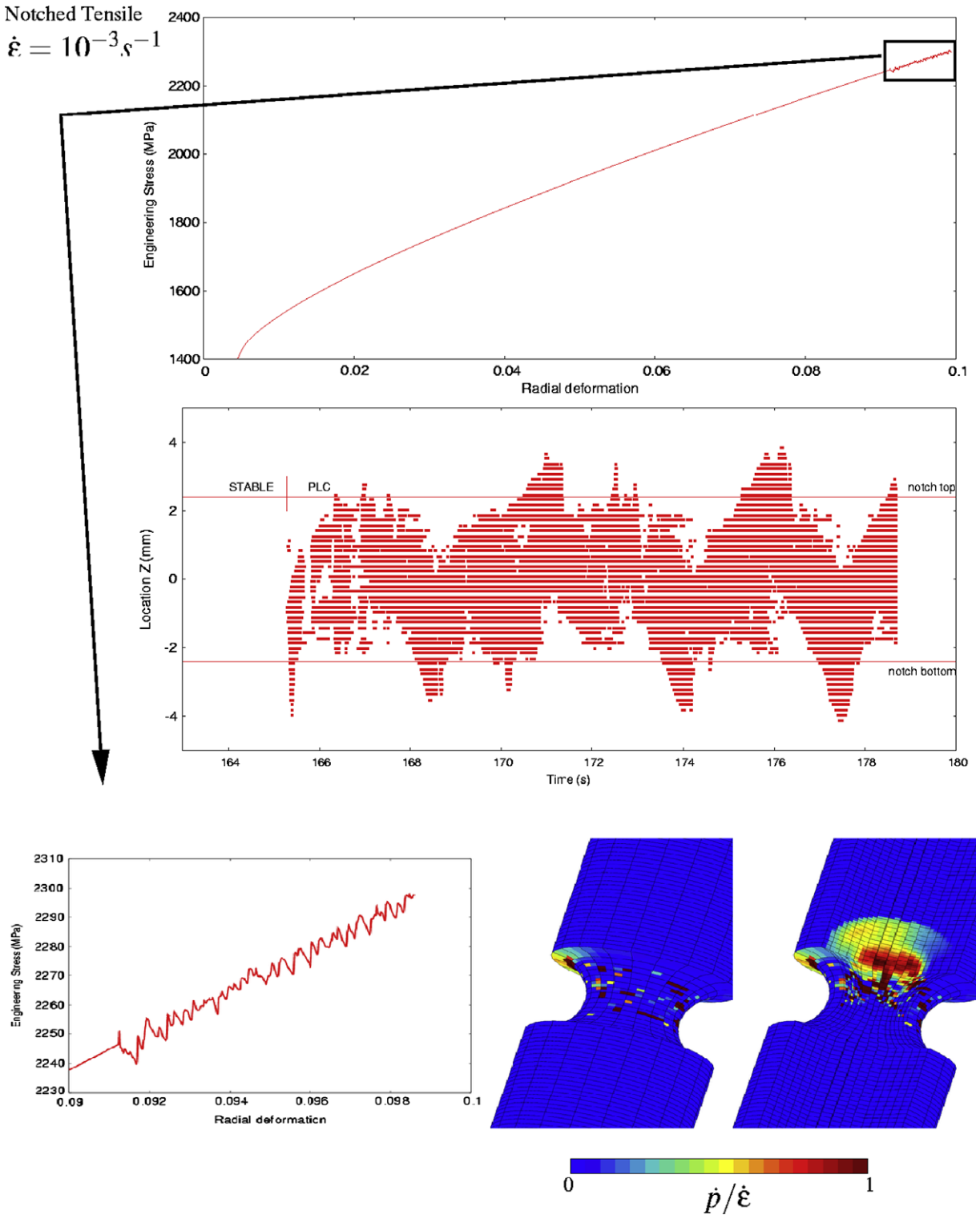

Fig. 22. Global engineering stress/strain curve, location of bands as a function of time, zoom on serrations and plastic strain rate in the specimen at $t = 176$ s for a notched axisymmetric specimen at a prescribed strain rate $\dot{\varepsilon} = 10^{-3}$ s^{-1}.

Figs. 18–20 show for each strain rate (10^{-2} s^{-1}, 10^{-4} s^{-1}, 10^{-6} s^{-1}): The global stress/strain curve with a zoom on serrations, a view of finite element solutions of the cumulated plastic strain rate $\dot{p}$, and the band location as a function of time provided by the band location indicator (BLI). Two plots for $\dot{p}$ are provided for each strain rate, the first is an external view of the whole specimen, the second one is a cross section view of half of the specimen in order to observe the internal band shapes. The type and shape of bands observed for each simulation can then be compared.

Band type A is observed for high strain rate values. In Fig. 18 ($\dot{\varepsilon} = 10^{-2}$ s^{-1}), two type A bands are propagating simultaneously, implying irregularities on their shapes and on serrations. Then for lower strain rates, type B bands begin to appear. Their shape is no longer regular like in Fig. 19 ($\dot{\varepsilon} = 10^{-4}$ s^{-1}). The corresponding serrations are still quite regular. On Fig. 20 ($\dot{\varepsilon} = 10^{-6}$ s^{-1}), bands hesitate between type B and C with short hopping propagation. They can nucleate at any time anywhere in the specimen.

5.4. Notch tensile specimens

Tensile tests on notched specimens are useful to investigate the influence of stress triaxiality on the mechanical behavior of a given material. Associated with tensile tests on smooth specimens, such experiments provide valuable information on the yield surface [54] or on the fracture behavior [12]. One can define the sharpness of the notch using the non-dimensional notch parameter n_0. If R_0 denotes the notch radius and d the ligament width (flat specimens) or diameter (cylindrical specimens), the notch parameter is $n_0 = 10R_0/d$. Specimens with smooth notches have a large notch parameter and sharp specimens a small one. In this work, the notch parameter of the simulated specimen is $n_0 = 4$.

Only few simulations of PLC effect on notched specimens are available in the literature. In [35], tensile tests on two flat specimens with smooth ($n_0 = 20$) and sharp ($n_0 = 0.5$) notches are simulated using 2D meshes and compared with experimental results. For the first specimen, serrations appear on both experimental and numerical stress versus radial deformation curves. Localization bands escape from the notch but remain close to it. For the sharp specimen, neither experimental or numerical stress versus radial deformation curves are serrated but one can observe during simulation the initiation and propagation of bands in the notch over short distances. In [8], two flat notched specimens are considered, one with $n_0 = 30$ and the other with $n_0 = 5$. Simulations are performed using 3D meshes. For both specimens, serrations are observed on experimental and numerical stress versus radial deformation curves. Simulations suggest that localization bands propagate out of the notch (especially for $n_0 = 5$) and in the whole specimens, while bands based on the experimental data always seem to propagate inside the notch. Finally, in [7] cylindrical specimens with three notch shapes corresponding to $n_0 = 3.33, n_0 = 1.33$, and $n_0 = 0.66$ are investigated. Simulations are carried out using 2D axisymmetrical meshes and compared with experimental results. Serrations are found on all experimental and numerical curves. Simulations result that localization bands stay in the notch for the smoother specimen ($n_0 = 3.33$), whereas for sharper ones ($n_0 = 1.33$, and $n_0 = 0.66$) bands seems to leave the notch and to propagate out of it.

In this work, containment of localization bands in the notch is investigated with respect to the global prescribed strain rate (cross head velocity divided by twice the initial notch radius). For that purpose, five simulations are carried out prescribing five different global strain rates: $\dot{\varepsilon} = 10^{-2}$ s^{-1}, 10^{-3} s^{-1}, 10^{-4} s^{-1}, 10^{-5} s^{-1}, 10^{-6} s^{-1}. Simulations are performed using full 3D meshes to model the cylindrical specimen defined in Section 5.1. Serrations arise on every stress versus radial deformation curves, and bands of localized plastic strain rate are observed for the five prescribed strain rates. The critical plastic strain, and the amplitude of serrations seem to follow the same evolution as for smooth specimens: The first one increases and the latter decreases when the prescribed strain rate increases. Band shapes inside specimens are drawn in Fig. 21 for each prescribed strain rate. One can observe that for low strain rates, bands are confined in the notch or just near it. For higher strain rates, they nucleate in the notch but can propagate away from it. For all prescribed strain rates, one can observe a full symmetry breaking of band pattern.

The global stress versus radial deformation curve and the BLI response of the simulation performed at $\dot{\varepsilon} = 10^{-3}$ s^{-1} are plotted on Fig. 22. The amplitude of serrations is almost the same than for smooth specimens. The BLI response suggests that the band nucleates at one side of the notch and propagate to its other edge. Then, the band tries to escape from the notch, but does not succeed to do so, and comes back into the notch as if it was fixed by a spring to the center of the notch. The notch holds the band captive. Results found in the literature and those presented in this work suggest that this containment of bands in the notch for cylindrical specimens is accentuated by low strain rates and sharp notches.

6. Conclusions

This work shows that the MC model can be used for reliable simulations of PLC phenomena in complex sample geometries. Typical features of the PLC effect are recovered in a reliable and robust way. For that purpose, a specific integration method has been proposed that switches from implicit to explicit local integration when severe instabilities are encountered. A new numerical tool to estimate the position of band with respect to time was introduced. A detailed mesh sensitivity analysis was performed, and some large scale simulations were performed. Four main new results were obtained in this work:

(1) Constitutive equations can be integrated using a mixed implicit/explicit formulation. Equations are mainly integrated using the Θ-method and sometimes using Runge–Kutta method, when the internal variables are subjected to too large variations. This method is actually faster than a pure explicit method to accurately simulate serrations of the Portevin–Le Chatelier effect.
(2) The BLI tool is accurate to locate at each time step the position of PLC bands. The type of bands in simulations has been determined drawing numerical spatio-temporal patterns (STP) reproducing those experimentally drawn using laser extensometry or infrared pyrometry. Some kinematics parameters of bands have also been estimated using this tool.
(3) The simulation results are found to be mesh dependent, but not for all variables. The width of bands and the maximal plastic strain rate are found to be mesh dependent, whereas their velocity or the amount of plastic strain carried are mesh insensitive. A non-local model, based on some experimental measures of bands width [62], would be however an interesting improvement for the MC model.
(4) The model implementation is robust enough to carry out large scale 3D simulations on smooth and notched tensile specimens for several strain rates. The type and shape of bands is found to be rate-dependent for both geometries. A lonely inclined band has been simulated for the first time in a 3D axisymmetric smooth specimen.

Many examples of PLC effect on tensile curves are available in the literature for several materials and specimens types. The comparison of band shape and type between experiment and simulations has not been performed yet, especially for 3D specimens.

Moreover, it has been shown that experimental shape and type of bands are not the same for flat smooth as for cylindrical smooth specimens [6]. Using the numerical tools developed in this work, a comparison of the shape and type of bands between experiments on flat specimens, experiments on cylindrical specimens, 2D simulations, and 3D flat and cylindrical simulations should be carried out in the future on other materials.

The mesh dependency of the PLC simulations has been evidenced in this work. Some regularization methods have to be investigated in order to limit this dependency. Simulation accounting for thermal effect or implicit dynamic calculation can be considered to solve this problem. The development of a non-local gradient model based on the MC one would be another solution.

The purely phenomenological approach of the simulation of strain ageing phenomena envisaged in the present work should be enriched in order to incorporate some aspects of their multiscale nature. The underlying dislocation avalanches can be related to the evolution of dislocation densities treated as internal variables. It would enable us to link strain ageing and material workhardening. An attempt to introduce such physically based constitutive equations for static strain ageing can be found in [5,4].

On the other hand, characteristic lengths related to grain size or typical intragranular strain localization patterns should be introduced in future versions of the model.

Finally, some experimental and numerical results present a link between the PLC effect and early fracture of specimens. In [40] simulations suggest that the PLC effect leads to significant reductions in the strain to necking. In [6], necking appears in a propagating band that stops at a given position in the steel specimen. Then, the simulation of rupture of material submitted to the PLC effect should be investigated to evaluate which part is due to strain ageing. Such an analysis would require a non-local finite strain elastoviscoplastic with damage model, in order to account for softening and rupture of specimens [12].

Acknowledgements

This work has been carried within the common project DDV leaded by ONERA (French Aeronautics and Space Research Center) and funded by the DGA (French Ministry of Defense) which is gratefully acknowledged.

References

[1] H. Ait-Amokhtar, C. Fressengeas, S. Boudrahem, The dynamics of Portevin–Le Chatelier bands in an Al–Mg alloy from infrared thermography, Mat. Sci. Engrg. 488 (2008) 540–546.
[2] H. Ait-Amokhtar, P. Vacher, S. Boudrahem, Kinematics fields and spatial activity of Portevin–Le Chatelier bands using the digital image correlation method, Acta Mater. 54 (2006) 4365–4371.
[3] N. Aravas, On the numerical integration of a class of pressure-dependent plasticity models, Int. J. Numer. Meth. Engrg. 24 (1987) 1395–1416.
[4] V. Ballarin, A. Perlade, X. Lemoine, O. Bouaziz, S. Forest, Mechanisms and modeling of bake-hardening steels: Part II. Complex loading paths, Metallurg. Mater. Trans. A – Phys. Metallurg. Mater. Sci. 40A (6) (2009) 1375–1382.
[5] V. Ballarin, M. Soler, A. Perlade, X. Lemoine, S. Forest, Mechanisms and modeling of bake-hardening steels: Part I. Uniaxial tension, Metallurg. Mater. Trans. A – Phys. Metallurg. Mater. Sci. 40A (6) (2009) 1367–1374.
[6] J. Belotteau, Prévision de la déchirure ductile des aciers au C-Mn en présence de vieillissement statique et dynamique, Ph.D. Thesis, Ecole Centrale Paris, 2009.
[7] A. Benallal, T. Berstad, T. Borvik, A. Clausen, O. Hopperstad, Dynamic strain aging and related instabilities: experimental, theoretical and numerical aspects, Eur. J. Mech. 25 (2006) 397–424.
[8] A. Benallal, T. Berstad, T. Borvik, O. Hopperstad, I. Koutiri, R. de Codes, An experimental and numerical investigation of the behavior of AA5083 aluminium alloy in presence of the Portevin–Le Chatelier effect, Int. J. Plasticity 24 (2008) 1916–1945.
[9] A. Benallal, T. Borvik, A. Clausen, O. Hopperstad, Dynamic strain aging, negative strain-rate sensitivity and related instabilities, Techn. Mech. 23 (2003) 160–166.
[10] A. Benallal, C. Comi, Localization analysis via a geometrical method, Int. J. Solid Struct. 33 (1996) 99–119.
[11] A. Bertram, Elasticity and Plasticity of Large Deformations, Springer, 2005.
[12] J. Besson, C. Berdin, S. Bugat, F. Feyel, Collectif, local approach to fracture, Ecole des Mines de Paris, 2004.
[13] J. Besson, G. Cailletaud, J.-L. Chaboche, S. Forest, Non Linear Mechanics of Materials, Springer, 2009.
[14] J. Besson, R. Foerch, Large scale object-oriented finite element code design, Comp. Meth. Appl. Mech. Engrg. 142 (1997) 165–187.
[15] J. Besson, D. Steglich, W. Brocks, Modeling of plane strain ductile rupture, Int. J. Plasticity 19 (10) (2003) 1517–1541.
[16] T. Böhlke, G. Bondar, Y. Estrin, M. Lebyodkin, Geometrically non-linear modeling of the Portevin–Le Chatelier effect, Comput. Mat. Sci. 44 (2009) 1076–1088.
[17] J. Chaboche, G. Cailletaud, Integration methods for complex plastic constitutive equations, Comp. Meth. Appl. Mech. Engrg. 133 (1996) 125–155.
[18] A. Chatterjee, A. Sarkar, S. Bhattacharya, P. Mukherjee, N. Gayathri, P. Barat, Markov property of continuous dislocation band propagation, Phys. Lett. A 372 (2008) 4016–4020.
[19] Z. Chen, Q. Zhang, Z. Jiang, H. Jiang, X. Wu, A macroscopic model for the Portevin–Le Chatelier effect, J. Mater. Sci. Technol. 20 (5) (2004) 535–539.
[20] F. Chmelik, F. Klose, H. Dierke, J. Sach, H. Neuhäuser, P. Lukac, Investigating Portevin–Le Chatelier effect in strain rate and stress rate controlled tests by the acoustic emission and laser extensometry techniques, Mat. Sci. Engrg. 426 (2007) 52–60.
[21] F. Chmelik, A. Ziegenbein, H. Neuhäuser, P. Lukac, Investigating Portevin–Le Chatelier effect by the acoustic emission and laser extensometry techniques, Mat. Sci. Engrg. 324 (2002) 200–207.
[22] M. Cieslar, C. Fressengeas, A. Karimi, J.-L. Martin, Portevin–Le Chatelier effect in biaxially strained Al–Fe–Si foils, Scripta Mater. 48 (2003) 1105–1110.
[23] A. Cottrell, A note on the Portevin–Le Chatelier effect, Phil. Mag. 44 (1953) 829–832.
[24] H. Dierke, F. Krawehl, S. Graff, S. Forest, J. Sachl, H. Neuhäuser, Portevin–Le Chatelier effect in Al–Mg alloys: influence of obstacles – experiments and modelling, Comput. Mat. Sci. 39 (2007) 106–112.
[25] H. Dybiec, M. Chaturvedi, Serrated yielding in Inconel 718, Arch. Metallurg. 36 (1991) 341–352.
[26] M. Fellner, M. Hamersky, E. Pink, A comparison of the Portevin–Le Chatelier effect in constant-strain-rate and constant-stress-rate tests, Mat. Sci. Engrg. 137 (1991) 157–161.
[27] R. Foerch, J. Besson, G. Cailletaud, P. Pilvin, Polymorphic constitutive equations in finite element codes, Comp. Meth. Appl. Mech. Engrg. 141 (1997) 355–372.
[28] L. Fournier, D. Delafosse, T. Magnin, Oxidation induced intergranular cracking and Portevin–Le Chatelier effect in nickel base superalloy 718, Mat. Sci. Engrg. 316 (2001) 166–173.
[29] S. Franklin, F. Mertens, M. Marder, Portevin–Le Chatelier effect, Phys. Rev. E 62 (2000) 8195–8206.
[30] C. Fressengeas, A. Beaudoin, M. Lebyodkin, L. Kubin, Y. Estrin, Dynamic strain aging: a coupled dislocation-solute dynamic model, Mat. Sci. Engrg. 400 (2005) 226–230.
[31] V. Garat, J. Cloue, D. Poquillon, E. Andrieu, Influence of Portevin–Le Chatelier effect on rupture mode of alloy 718 specimens, J. Nucl. Mater. 375 (2008) 95–101.
[32] G. Girardin, D. Delafosse, Measurement of the saturated dislocation pinning force in hydrogenated nickel and nickel base alloys, Scripta Mater. 51 (2004) 1177–1181.
[33] P. Gomiero, Y. Brechet, F. Louchet, A. Tourabi, B. Wack, Microstructure and mechanical-properties of a 2091 AlLi alloy – III. Quantitative analysis of Portevin–Le Chatelier instabilities and relation to toughness in Al–Li, Al–Cu–Li and Al–Li–Cu–Mg (2091) alloys, Acta Metal. Mater., 40 (1992) 863–871.
[34] S. Graff, H. Dierke, S. Forest, H. Neuhäuser, J.-L. Strudel, Finite element simulations of the Portevin–Le Chatelier effect in metal–matrix composites, Phil. Mag. 88 (2008) 3389–3414.
[35] S. Graff, S. Forest, J.-L. Strudel, C. Prioul, P. Pilvin, J.-L. Béchade, Strain localization phenomena associated with static and dynamic strain ageing in notched specimen: experiments and finite element simulations, Mat. Sci. Engrg. 387 (2004) 181–185.
[36] S. Graff, S. Forest, J.-L. Strudel, C. Prioul, P. Pilvin, J.-L. Béchade, Finite element simulations of dynamic strain ageing effects at V-notches and crack tips, Scripta Mater. 52 (2005) 1181–1186.
[37] P. Hähner, E. Rizzi, On the kinematics of Portevin–Le Chatelier bands: theoretical and numerical modelling, Acta Mater. 51 (2003) 3385–3397.
[38] H. Halim, D. Wilkinson, M. Niewczas, The Portevin–Le Chatelier (PLC) effect and shear band formation in an AA5754 alloy, Acta Mater. 55 (2007) 4151–4160.
[39] O. Hopperstad, T. Borvik, T. Berstad, A. Benallal, Finite element simulations of the Portevin–Le Chatelier effect in aluminium alloy, J. Phys. IV 134 (2006) 435–441.
[40] O. Hopperstad, T. Borvik, T. Berstad, . Lademo, A. Benallal, Numerical study on the influence of the Portevin–Le Chatelier effect on necking in an aluminium alloy, Model. Simul. Mater. Sci. Engrg. 15 (2007) 747–772.
[41] H. Jiang, Q. Zhang, X. Chen, Z. Chen, Z. Jiang, X. Wu, J. Fan, Three types of Portevin–Le Chatelier effect: experiment and modelling, Acta Mater. 55 (2007) 2219–2228.
[42] J. Kang, D. Wilkinson, M. Jain, J. Embury, A. Beaudoin, S. Kim, R. Mishira, A. Sachdev, On the sequence of inhomogeneous deformation processes occurring during tensile deformation of strip cast AA5754, Acta Mater. 54 (2006) 209–218.

[43] S. Kok, M. Bharathi, A. Beaudoin, C. Fressengeas, G. Ananthakrishna, L. Kubin, M. Lebyodkin, Spatial coupling in jerky flow using polycrystal plasticity, Acta Mater. 51 (2003) 3651–3662.
[44] Z. Kovacs, J. Lendvai, G. Voros, Localized deformation bands in Portevin–Le Chatelier plastic instabilities at a constant stress rate, Mat. Sci. Engrg. 279 (2000) 179–184.
[45] L. Kubin, Y. Estrin, The Portevin–Le Chatelier effect in deformation with constant stress rate, Acta Metallurg. 33 (1985) 397–407.
[46] A. Le Chatelier, Influence du temps et de la température sur les essais au choc, Rev. Métallurg. 6 (1909) 914–917.
[47] M. Lebyodkin, L. Dunin-Barkowskii, Y. Brechet, Y. Estrin, L. Kubin, Spatio-temporal dynamics of the Portevin–Le Chatelier effect: experiment and modelling, Acta Mater. 48 (2000) 2529–2541.
[48] M. Lebyodkin, Y. Estrin, Multifractal analysis of the Portevin–Le Chatelier effect: general approach and application to AlMg and AlMg/Al_2O_3 alloys, Acta Mater. 53 (2005) 3403–3413.
[49] H. Louche, Chrysochoos, Thermal and dissipative effects accompanying Lüders band propagation, Mat. Sci. Engrg. 307 (2001) 15–22.
[50] H. Louche, P. Vacher, R. Arrieux, Thermal observations associated with the Portevin–Le Chatelier effect in an Al–Mg alloy, Mat. Sci. Engrg. 404 (2005) 188–196.
[51] M. Mazière, Overspeed burst of turbo engine disks, Ph.D. Thesis, Mines ParisTech, 2007.
[52] M. Mazière, J. Besson, S. Forest, B. Tanguy, H. Chalons, F. Vogel, Numerical modelling of the Portevin–Le Chatelier effect, Eur. J. Computat. Mech. 17 (2008) 761–772.
[53] M. Mazière, J. Besson, S. Forest, B. Tanguy, H. Chalons, F. Vogel, Overspeed burst of elastoviscoplastic rotating disks – Part I: Analytical and numerical stability analyses, Eur. J. Mech. 28 (2009) 36–44.
[54] M. Mazière, J. Besson, S. Forest, B. Tanguy, H. Chalons, F. Vogel, Overspeed burst of elastoviscoplastic rotating disks – Part II: Burst of a superalloy turbine disk, Eur. J. Mech. 28 (2009) 428–432.
[55] P. McCormick, Theory of flow localization due to dynamic strain ageing, Acta Metallurg. 36 (1988) 3061–3067.
[56] S. Mesarovic, Dynamic strain aging and plastic instabilities, J. Mech. Phys. Solid 43 (1995) 671–700.
[57] A. Miserez, A. Mortensen, Fracture of aluminium reinforced with densely packed ceramic particles: influence of matrix hardening, Acta Mater. 52 (2004) 5331–5345.
[58] P. Penning, Mathematics of the Portevin–Le Chatelier effect, Acta Metallurg. 20 (1972) 1169–1175.
[59] A. Portevin, F. Le Chatelier, Sur le phénomène observé lors de l'essai de traction d'alliages en cours de transformation, C.R. Acad. Sci. Paris 176 (1923) 507–510.
[60] W. Press, S. Teukolsky, W. Vetterling, B. Flannery, Numerical Recipes in C, Cambridge University Press, 1992.
[61] N. Ranc, D. Wagner, Some aspects of Portevin–Le Chatelier plastic instabilities investigated by infrared pyrometry, Mat. Sci. Engrg. 394 (2005) 87–95.
[62] N. Ranc, D. Wagner, Experimental study by pyrometry of Portevin–Le Chatelier plastic instabilities – Type A to type B transition, Mat. Sci. Engrg. 474 (2008) 188–196.
[63] K. Rao, S. Kalluri, G. Halford, M. McGaw, Serrated flow and deformation substructure at room-temperature in Inconel 718 superalloy during strain controlled fatigue, Scripta Metallurg. Mater. 32 (1995) 493–498.
[64] J. Rice, The localisation of plastic deformation, in: W. Koiter (Ed.), Proceedings of the 14th International Conference Theoretical and Applied Mechanics, Delft, North–Holland, Amsterdam, 1976, pp. 207–220.
[65] E. Rizzi, P. Hähner, On the Portevin–Le Chatelier effect: theoretical and numerical results, Int. J. Plasticity 20 (2004) 121–165.
[66] A. Sarkar, C. Webber, P. Barat, P. Mukherjee, Recurrence analysis of the Portevin–Le Chatelier effect, Phys. Lett. A 372 (2008) 1101–1105.
[67] F. Sidoroff, A. Dogui, Some issues about anisotropic elastic–plastic models at finite strain, Int. J. Solid Struct. 38 (2001) 9569–9578.
[68] J. Simo, R. Taylor, Consistent tangent operators for rate-independent elastoplasticity, Comp. Meth. Appl. Mech. Engrg. 48 (1985) 110–118.
[69] J. Strudel, Interactions between dislocations and impurities, in: Japan–France Seminar on Fundamental Aspects of Mechanical Properties and Microstructure Evolution of Stainless Steels at High Temperature, Tokyo, 1984, pp. 169–180.
[70] G. Touzot, J. Dabounou, Intégration numérique de lois de comportement élastoplastique, Rev. Eur. Elémen. Finis 2 (1993) 465–494.
[71] H. Tsukahara, T. Iung, Piobert–Lüders and Portevin–Le Chatelier instabilities. Finite element modelling with abaqus, J. Phys. IV 9 (1999) 157–164.
[72] A. van den Beukel, Theory of the effect of dynamic strain ageing on mechanical properties, Phys. Status Solidi 30 (1975) 197–206.
[73] H. Zbib, E. Aifantis, On the localization and postlocalization behavior of plastic deformation. III. On the structure and velocity of the Portevin–Le Chatelier bands, Res. Mech. 23 (1988) 293–305.
[74] S. Zhang, P. McCormick, Y. Estrin, The morphology of Portevin–Le Chatelier bands: finite element simulation for Al–Mg–Si, Acta Mater. 49 (2001) 1087–1094.